Soil Dynamics and Earthquake Engineering, 2019, Vol. 117, pp. 1-15, DOI: 10.1016/j.soildyn.2018.11.005

On the influence of platy shell particles on the cumulative deformations in sand under drained high-cyclic loading

T. Wichtmann[i] ; Th. Triantafyllidis[ii]; L. Ziesmann[iii]

Abstract: Mixtures of a fine sand with platy shell fragments have been tested under drained monotonic and high-cyclic loading. The content (0 to 40 %) and the size of the platy shell particles in the mixtures were varied. Comparative tests have been also performed on a mixture containing 40 % coarse sand and gravel particles instead of the shells. In the cyclic tests different stress amplitudes, initial relative densities and average stresses have been tested on the various mixtures. The strain accumulation rates were found to increase with growing content of shell particles. This can be primarily attributed to the more well-graded grain size distribution curves of the sand-shell mixtures. Particle breakage effects were almost absent in the cyclic tests as demonstrated by sieve analysis. Dependencies between the parameters of a high-cycle accumulation (HCA) model and the content of shell particles are analyzed. Amongst others, an extraordinary low dependence of the strain accumulation rate on strain amplitude (parameter $C_{\mathrm{ampl}} < 1$) has been observed for larger amounts of shell particles in the mixtures.

Keywords: high-cyclic loading; sand; platy shell fragments; drained cyclic triaxial tests; HCA model

1 Introduction

Offshore wind turbines (OWT) are usually founded on piles (monopiles, tripods, tripiles, jackets) or gravity base foundations. During their lifetime these foundations are subjected to a large number of cycles caused by wind and waves (so-called high-cyclic loading). The cyclic loading may lead to an accumulation of deformations in the subsoil, resulting in differential settlements and a tilting of the structure. The tilting has to be kept within small tolerances ($\theta < 0.5°$), however, to guarantee serviceability. The permanent deformations of the OWT foundations thus have to be accurately predicted during the design phase.

Finite element calculations with the high-cycle accumulation (HCA) model of Niemunis et al. [65] may be performed for that purpose. The procedure for OWT monopile foundations is explained in detail in [103]. All previous drained cyclic tests performed in order to develop the HCA model equations [102, 104–107] or a simplified calibration procedure based on granulometry [108–110] were restricted to clean quartz sands.

Marine sands, however, often contain a certain amount of potentially crushable particles, i.e. fragments of shells, corals or the remains of skeletons of other marine organisms. The experimental study presented in this paper is dedicated to a fundamental investigation on how such particles, in particular platy shell fragments, influence the cumulative response of sand under a drained high-cyclic loading and consequently the parameters of the HCA model. The effect of the amount, size and shape of the shell particles in a fine sand matrix on strain accumulation is studied for the first time. The response of the various mixtures to drained monotonic loading is inspected as well.

[i] Professor for Geotechnical Engineering, Bauhaus-Universität Weimar, Germany (corresponding author). Email: torsten.wichtmann@uni-weimar.de

[ii] Professor and Director of the Institute of Soil Mechanics and Rock Mechanics (IBF), Karlsruhe Institute of Technology (KIT), Germany

[iii] Master student, IBF, KIT, Germany

The following literature review briefly summarizes previous work on the influence of the particle characteristics on the behaviour of granular soils under either monotonic or cyclic loading with either drained or undrained conditions. The discussion includes the influences of grain size and gradation, fines content, grain shape, shell fragments and other potentially crushable particles.

2 Literature review

2.1 Influence of grain size

Although experimental studies dealing with the influence of mean grain size d_{50} on the sand response to monotonic loading are rare in the literature, there is a general consensus that the shear strength increases with d_{50}. A significant growth of the peak friction angle by $\Delta\varphi_P = 7°$ between d_{50} = 6.3 and 76.2 mm was reported by Al-Hussaini [2], based on tests on crushed basalt. However, in [2] both d_{50} and the uniformity coefficient $C_u = d_{60}/d_{10}$ (from 3.3 to 11.6) were increased simultaneously, i.e. both effects cannot be clearly distinguished. A slight trend for φ_P to increase with d_{50} is mentioned by Andersen & Schjetne [6], based on the compilation of data collected for numerous granular materials. In a systematic study on specially mixed sands and gravels with d_{50} values between 0.1 mm and 6 mm and constant C_u = 1.5 conducted by Wichtmann [103] the difference $\Delta\varphi_P$ between the finest and the coarsest material was found to decrease with growing density ($\Delta\varphi_P = 4°$ for loose and medium dense sand, $\Delta\varphi_P = 2°$ for dense sand).

Several studies with undrained cyclic loading revealed an increase of the liquefaction resistance with increasing mean grain size [15, 24, 25, 79, 80, 96, 103] for constant relative density. Parts of this increase may be, however, attributed to membrane penetration effects [64, 94, 95], which become more pronounced for larger particle sizes. The d_{50}-dependence of the undrained cyclic strength CRR (= cyclic resistance ratio) is corroborated by the observation from numerous laboratory studies that gravelly materials show a higher liquefaction resistance than sands [32, 39, 112].

The decrease of the rate of pore water pressure accumulation with increasing mean grain size observed for the undrained case is in good accordance with the results from drained long-term cyclic tests ($N = 10^5$ cycles), where a reduction of the rate of strain accumulation with growing d_{50} was found [103,110]. This conclusion is based on a systematic experimental investigation on sands and gravels with grain sizes in the range 0.1 mm $\leq d_{50} \leq$ 3.5 mm, while C_u = 1.5 was kept constant.

2.2 Influence of grading

The few respective experimental studies in the literature did not find a correlation between the shear strength and the uniformity coefficient C_u of a sand [6, 42]. An investigation of Wichtmann on specially mixed sands with $1.5 \leq C_u \leq 8$ and constant $d_{50} = 0.6$ mm came to the same conclusion [103]. While the initial stiffness in the drained monotonic triaxial tests was found to be rather unaffected by the uniformity coefficient as well, the dilatancy was less pronounced for the more well-graded materials [103].

The literature is inconsistent regarding the influence of the uniformity coefficient on the liquefaction resistance. According to some publications, well-graded soils are generally less susceptible to liquefaction than poorly graded ones [45,73,79]. Carraro et al. [13] stated that field evidence indicates that most liquefaction failures have involved uniformly graded soils. Andersen [5], however, did not find any clear trend when the undrained cyclic strength of various sands was plotted versus C_u. Likewise, neither Vaid et al. [100] nor Kokusho et al. [43] could find notable differences in the liquefaction resistance of specially mixed sands having different C_u values in case a constant relative density was considered. In contrast, Wichtmann [103] found a remarkable decrease of the undrained cyclic strength with increasing uniformity coefficient in tests on the specially mixed quartz sands mentioned above ($1.5 \leq C_u \leq 8$, d_{50} = 0.6 mm). This trend is in accordance with the higher strain accumulation rates measured for the more well-graded materials in drained long-term cyclic tests [103, 110], performed on the same granular materials.

2.3 Influence of fines content

While mixtures of a sand with coarser particles like gravel grains or shell fragments have rarely been investigated in the literature, a huge amount of studies on mixtures of sand and fines has been published. The fines are defined as particles with sizes less than 0.074 mm or 0.063 mm, depending on the standard code applied. The addition of fines to a coarser material usually results in a gap-graded mixture. The present literature review concentrates on non-plastic fines, i.e. silt.

The conclusions regarding the effect of the fines content FC on the material response to monotonic loading depend on the basis of comparison (constant void ratio e, skeleton or equivalent void ratio e^* or relative density I_D?). However, even if the same criterion is applied for comparison, the findings in the literature are not consistent. At similar relative density, some authors report about a decrease of initial stiffness (under drained conditions) [103] and an increase of dilatancy [50, 77] and shear strength [14,50,77] with increasing fines content, while others found the material response to render more contractive [11,14,26,48,103,117,118] (partly even at increasing relative density). Some authors observed a more pronounced dilatancy for higher values of fines content when a constant skeleton void ratio was considered (e.g. [46]), while it was the other way around in other studies (e.g. [19]). The larger compressibility of materials with fines at loose states is sometimes explained with a highly unstable structure since larger grains are hold slightly apart by silt particles near the contact points [30, 48, 90, 116–118]. When this metastable structure is subjected to shear stresses, the silt particles are forced into the void spaces, generating large contractive volumetric strains. Numerous authors have found a shift of the steady or critical state line in the e-ln(p) space with increasing fines content of the sand-silt mixture [8,10,12,22,34–36,59,60,63,67,70,72,86,91,93,119,121]. A coincidence of the critical state lines in a e^*-ln(p) diagram is reported in [22, 35, 58, 63, 71, 72, 92, 93, 121], partly achieved by choosing appropriate equations for the parameter b of $e^* = \frac{e+(1-b)FC}{1-(1-b)FC}$, describing the fraction of fines participating in the force transmission in the skeleton. Some authors define a transitional fines content, where the sand-dominated behaviour passes to a fines-dominated one [91,92,120,121]. At high fines contents (e.g. $FC \geq 40\%$) the material behaviour is dominated by the fines [116], with the coarser grains floating in the matrix of the fines.

Considering a constant relative density and a range of fines content between 0 and 20 %, either an increase of the liquefaction resistance with FC [4, 44, 103], no significant FC dependence [68] or a decrease with FC [7, 9, 17, 47, 85] was reported in the literature based on undrained cyclic tests. Sometimes, an initial rise of the curve $CRR(FC)$ up to a maximum between FC = 5 and 30 % was followed by a reduction at larger FC values (e.g. [13]). The opposite trend has been also documented [33]. In [41] the initial decrease was followed by almost constant CRR values. Comparing CRR at a constant void ratio, with some exceptions [4], almost all studies in the literature found a continuous decrease of the liquefaction resistance with increasing fines content [7, 12, 13, 17, 33, 35, 46, 67–69, 85–87, 98, 113]. A few studies reported about a re-increase of CRR for e = constant at larger FC values [41, 92]. For a constant skeleton or equivalent void ratio some authors found an increase of the undrained cyclic strength with increasing FC [13,46,67,68,86,87], while some others reported the opposite trend [85] or no effect of FC at all [35, 68, 92]. Some researchers observed a reduction up to a certain fines content followed by a re-increase at higher FC-values [22, 33].

The inconsistent conclusions in the literature give hints that the nature of the particles of the fine [26, 101, 119] and coarse particles, in particular their shape seem to play an important role and need further investigations in future.

2.4 Influence of particle shape

It is well known that the shear strength of a granular material increases with increasing angularity and surface roughness of the particles [6,16,18,28,29,40,42,52,56,57,66,74,75, 81, 82, 84, 88, 89, 103, 115, 122], due to the higher interparticle friction and interlocking between adjacent particles. A simultaneous reduction of packing density and stiffness [18, 57, 84, 103] and an increase in dilatancy [52, 97, 103, 122] are also reported in the literature.

Based on DSS tests with constant volume Vaid et al. [99] have demonstrated that the influence of the particle shape on the liquefaction resistance depends on pressure

and density. At lower vertical stresses ($\sigma'_{v0} = 200$ kPa) the undrained cyclic strength of angular sand exceeded that of rounded sand at any tested relative density. The same trend was observed at higher stress levels ($\sigma'_{v0} \geq 800$ kPa) in case of low densities. In contrast, for combinations of high stresses and high densities the liquefaction resistance of the angular sand was much lower than that of the rounded material. In [99] this is attributed to particle breakage effects. In [1] a similar liquefaction resistance for two sands with angular or sub-rounded grains at e = constant and $p_0 = 200$ kPa is reported. Taking into account the increase of the minimum and maximum void ratios $e_{\min}$ and $e_{\max}$ with angularity, this means a higher undrained cyclic strength for the angular material if a constant relative density I_D is considered. Based on a study with undrained cyclic tests started at $p_0 = 100$ kPa Wichtmann [103] came to the same conclusion, i.e. the liquefaction resistance of a crushed sand was observed to exceed that of a natural sand.

In drained tests with a large number of cycles ($N = 10^5$) conducted by Wichtmann [103] a similar pressure-dependence as reported by Vaid et al. [99] was detected. At low average mean effective stresses ($p^{\mathrm{av}} = 50$ kPa) the rate of strain accumulation was significantly higher for a mixture of glass beads than for a natural sand havint the same grain size distribution curve. The cumulative rates in a crushed sand were even lower. In contrast, at a higher pressure ($p^{\mathrm{av}} = 300$ kPa) all three materials showed similar residual strains. While particle breakage was negligible in this test series, the observations may be explained with elastic and plastic deformations at the particle contacts caused by the pressure increase, which render the contact behaviour independent of its original shape.

2.5 Influence of shell fragments and other crushable particles

Marine sands may be partly or completely composed of potentially crushable particles. These particles, which are fragments of shells, corals or the remains of skeletons of other marine organisms, are more angular and irregular than quartz grains, leading to a higher porosity of the grain skeleton and an improved interlocking between adjacent particles.

Several experimental studies with monotonic loading applied to sands partly or completely composed of particles being more susceptible to grain crushing than quartz grains are documented in the literature. In the majority calcareous or carbonate sands or granular materials of volcanic origin have been tested. Due to the more angular and irregular particles, the peak or residual shear strength [20, 83] and compressibility [27, 38, 83] of such granular materials are usually reported to be higher than for quartz sands. Only few studies found the opposite tendency, i.e. a decrease of shear strength with increasing crushability of the sand [57]. Giretti et al. [27] observed a higher residual friction angle of a carbonate sand compared to silica sands, while the lower peak friction angle was explained by a less pronounced dilatancy.

It could be expected that crushable sands show larger cumulative rates, not only because of particle breakage but also attributed to the higher void ratios and larger compressibility. However, several studies in the literature with undrained cyclic loading have found the opposite tendency. Crushable sands do not liquefy as easily as harder-grained sands of same density (e.g. [27,37,38,76]), primarily due to their more angular particle shape and related interlocking effects, hindering particle reorientations during undrained cyclic loading. The opposite behaviour, i.e. a higher liquefaction susceptibility for crushable sands compared to harder-grained materials has been, however, sometimes observed at higher densities and larger stresses [38, 76]. The latter may be attributed to the larger amount of particle breakage occurring at elevated pressure levels. Tests with drained cyclic loading performed on carbonate sands are documented in [23, 53].

The amount of particle crushing during monotonic loading has been found dependent on stress level, void ratio and particle characteristics (size, grading, shape, strength, mineral composition) [3, 20, 21, 31, 49, 51, 55, 61, 62, 114]. It is usually quantified by a comparison of pre- and post-test grain size distribution curves determined by sieve analysis, evaluating Hardin's relative breakage ratio B_r [31]. Beside the self-evident increase with pressure, grain crushing is more pronounced in uniformly graded than in well-graded sands [3, 21, 62]. Some studies on calcareous sands (e.g. [23]) report a considerable breakage of particles due to cyclic loading. It grows with increasing number of cycles and correlates with the permanent volumetric strain. Based on DEM simulations, Donohue et al. [23] gave a possible micromechanical explanation of the grain crushing mechanism occurring during cyclic loading. These simulations showed that the contact force network within a sample evolves with the number of cycles. Since different particles participate in the mostly loaded force chains during the cyclic loading, new particles will experience crushing. In contrast, negligible breakage was observed in other experimental work with cyclic loading of granular materials composed of potentially breakable particles [53, 76, 78].

A systematic experimental investigation on the behaviour of mixtures of sand with platy shell particles under monotonic and in particular drained high-cyclic loading is missing in the literature. Such study is documented in the following.

3 Tested materials and sample preparation procedure

Mixtures of Karlsruhe fine sand (KFS) with shell fragments have been tested in the present study. The shell fragments have been obtained by crushing North sea shells (Figure 1a), primarily originating from cockles and being rather hard. Three mixtures with 10, 20 or 40 % of relatively coarse shell fragments (90 % grain sizes in the range 0.6 mm $\leq d \leq$ 8 mm, mixtures denoted as SH10, SH20 and SH40) and a fourth one with 20 % finer shell particles (90 % within 0.2 mm $\leq d \leq$ 2 mm, SH20F) have been produced. The grain size distribution curves of Karlsruhe fine sand, of the pure shell fragments (after crushing) and the sand-shell mixtures are provided in Figure 2. For comparison, tests have been also performed on another mixture (G40) possessing the same grain size distribution curve as SH40 but with the coarse particles composed of subangular and compact natural coarse sand and fine gravel grains instead of the platy shell fragments.

The index properties of all tested materials are summarized in Table 1. The minimum and maximum densities of the various mixtures have been determined according to German standard code DIN 18126. The minimum density

Fig. 1: Photos of a) the shells before crushing, b) mixture SH40 of Karlsruhe fine sand with 40 % crushed shell particles and c) mixture G40 of Karlsruhe fine sand with 40 % coarse sand or gravel particles

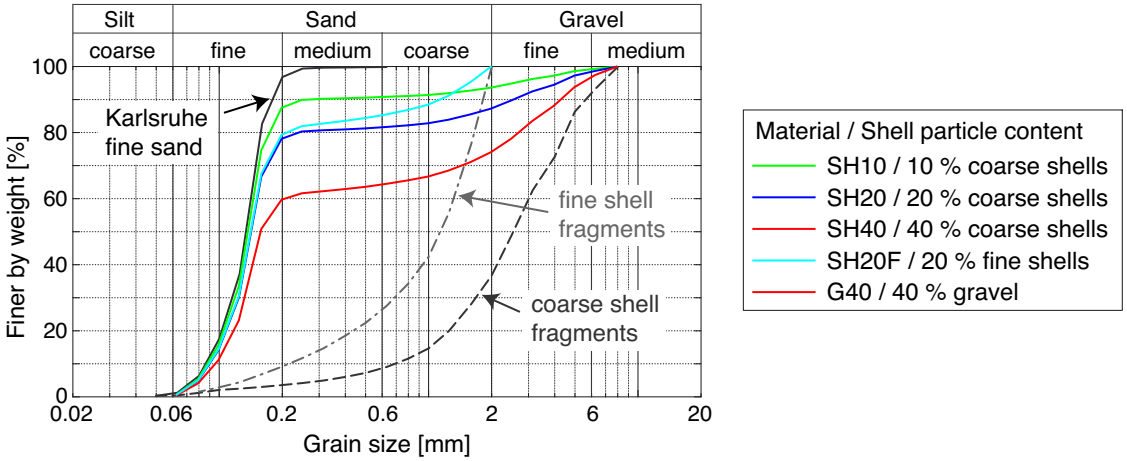

Fig. 2: *Grain size distribution curves of Karlsruhe fine sand, the pure crushed shell fragments and the mixtures of sand with shell fragments*

was obtained from loose placement of the oven-dried material in a cylinder by means of a funnel. The maximum density was measured in a test with layerwise compaction of the material under water. The latter testing method was applied despite the fact that the content of fine sand of the mixtures exceeds the limit of 50 % specified by DIN 18126. For gap-graded materials like the mixtures in the present study this method is preferable to the compaction on a shaking table because the latter procedure may lead to segregation. Photos of the mixtures SH40 and G40 are provided in Figure 1b,c.

All triaxial samples tested in the present study were prepared by air pluviation. Although some segregation will inevitably occur, the air pluviation method has been chosen to reproduce the deposition of the sand under offshore conditions. The impact of the sample preparation method has been studied on the pure Karlsruhe fine sand (see a documentation in [103, 111]), but not on the sand-shell mixtures. During the sample preparation the platy shell particles tend to be deposited with an orientation in the horizontal direction. This effect is more pronounced in case of the larger shell particlesand for higher densities. During the preparation of loose samples the larger discharge rate of the sand hinders the horizontal orientation of the shell particles. Therefore, it can be assumed that the loose samples show a somewhat more random orientation of the shell particles. It is possible that some kind of macropores develop during sample preparation, when the shell particles bridge holes in the uneven actual sand surface. The macropores will partly or fully disappear during the subsequent increase of the effective stress. As discussed later, the results of the cyclic tests on the various mixtures give hints that such macropores are absent or at least play only a minor role regarding the cumulative response of the mixtures. Micromechanical investigations on these issues have not been performed so far, but are planned for the future.

4 Monotonic tests

Prior to the cyclic tests some drained triaxial tests with monotonic loading have been performed on the clean sand and the various mixtures for reference purpose. A standard triaxial device was used for that purpose. Each material has been tested with different initial densities. The samples measured 10 cm in diameter and 10 cm in height. Smeared end plates were used to reduce end friction effects. After preparations the samples were saturated with de-aired water. A back pressure of 500 kPa was applied in all tests. The quality of saturation was checked by Skempton's B-value. B-values larger than 0.99 were achieved in all tests. The shearing was started from an isotropic state of stress with an effective mean stress of $p_0 = 100$ kPa (with $p = (\sigma'_1 + 2\sigma'_3)/3$). Keeping cell pressure constant, the samples were sheared with a displacement rate of 0.1 mm/min in the axial direction.

The diagrams in Figure 3a,b present the curves of deviatoric stress $q = \sigma_1 - \sigma_3$ and volumetric strain $\varepsilon_v = \varepsilon_1 + 2\varepsilon_3$ for loose and dense sand as functions of axial strain ε_1. Sev-

Material	FC [%]	d_{50} [mm]	C_u [-]	Percent of shell fragments	Percent of coarse sand and gravel	$e_{\min}$ [-]	$e_{\max}$ [-]	ϱ_s [g/cm^3]
Karlsruhe fine sand (KFS)	0.9	0.14	1.5	-	-	0.677	1.054	2.65
SH10	0.9	0.14	1.7	10 % coarse	-	0.654	1.008	2.67
SH20	0.8	0.14	1.7	20 % coarse	-	0.621	0.908	2.69
SH40	0.6	0.16	2.1	40 % coarse	-	0.498	0.737	2.71
SH20F	0.8	0.14	1.7	20 % fine	-	0.653	0.958	2.69
G40	0.6	0.16	2.1	-	40 %	0.479	0.691	2.64

Table 1: Index properties (fines content FC, mean grain size d_{50}, uniformity coefficient $C_u = d_{60}/d_{10}$, shell particle content, content of coarse sand and gravel, minimum and maximum void ratios $e_{\min}$ und $e_{\max}$, grain density ϱ_s) of the tested materials

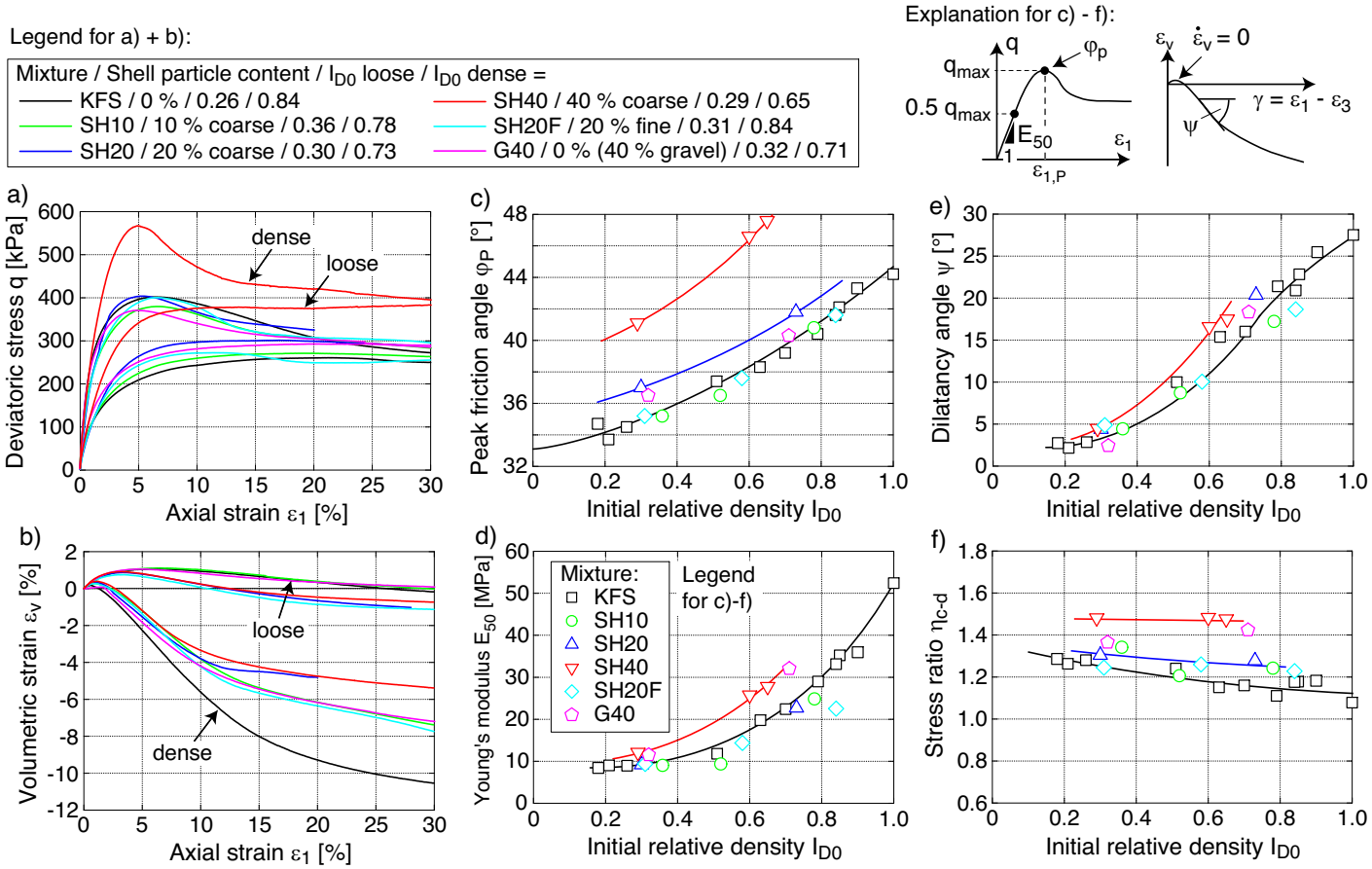

Fig. 3: *Results of drained monotonic triaxial tests: a,b) Curves $q(\varepsilon_1)$ and $\varepsilon_v(\varepsilon_1)$ for loose and dense samples, c) Peak friction angle φ_P, d) Young's modulus E_{50}, e) dilatancy angle ψ and f) stress ratio η_{c-d} at the onset of dilatancy as functions of initial relative density I_{D0}*

eral quantities derived from these curves are plotted versus the initial relative density $I_{D0} = (e_{\max} - e_0)/(e_{\max} - e_{\min})$ in Figure 3c-f. The initial density describes the state of the sample prior to shearing. Only the mixtures SH20 and SH40 with 20 or 40 % coarse shell fragments show a higher peak shear strength than the original Karlsruhe fine sand (Figure 3a,c). In those cases the platy shell particles seem to act as a kind of reinforcement, impeding the development of shear zones. This effect seems to be of minor importance for lower percentages of shell fragments in the mixture (SH10) and for finer shell particles (SH20F). Since the mixture G40 with the coarse fraction composed of subangular sand and gravel grains shows a similar shear strength than the original KFS (Figure 3a,c), the higher peak friction angles φ_P of SH20 and in particular SH40 can clearly be attributed to the platy shape of the particles within these mixtures.

Furthermore, the diagrams in Figure 3d-f reveal that larger amounts of coarse shell fragments lead to a moderate increase in the Young's modulus E_{50} (defined as a secant stiffness between $q = 0$ and $q = q_{\max}/2$), slightly higher dilatancy angles ψ and considerably larger stress ratios at the onset of dilatancy η_{c-d}, with $\eta = q/p$. The latter tendency seems to be partially related to the higher non-uniformity of the grain size distribution curve rather than to the platy particle shape, since the η_{c-d} data for SH40 and G40 are similar, at least at larger densities.

5 Cyclic tests

A scheme of the cyclic triaxial device used for the present study is shown in Figure 4. In this device the axial loading

is applied by means of a pneumatic cylinder mounted below the pressure cell. The axial force is measured at a load cell being located directly below the bottom end plate of the sample, i.e. inside the pressure cell. The axial deformation is obtained from a displacement transducer attached to the load piston. The system compliance was determined in preliminary tests on a steel dummy and subtracted from the measured values. Volume changes are determined via the pore water being sucked in or squeezed out from the sample, using a burette system and a differential pressure transducer (not shown in Figure 4). Two pressure transducers are applied for monitoring cell pressure and back pressure. The data of all transducers is continuously recorded by a data acquisition system.

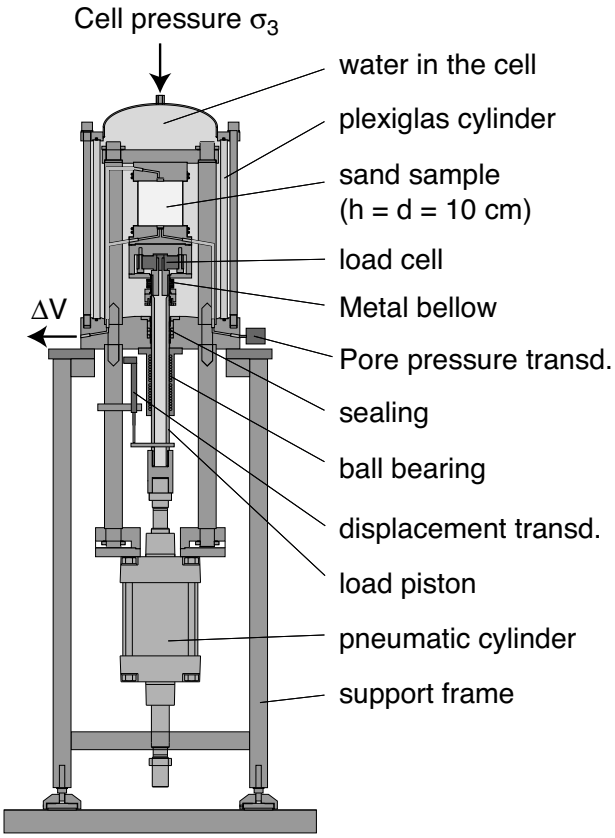

Fig. 4: *Scheme of the cyclic triaxial device used for this study*

The sample geometry and the sample preparation procedure in the cyclic tests were the same as in case of the monotonic tests. Following the B value test, the desired average stress (average mean pressure p^{av}, average stress ratio $\eta^{av} = q^{av}/p^{av}$) was applied and kept constant for one hour. Afterwards the cyclic axial loading with a stress amplitude $q^{ampl} = \sigma_1'^{ampl}$ was started (Figure 5a). Due to the larger deformations (Figure 5b) the first *irregular* cycle was applied with a low loading frequency of 0.01 Hz, in order to prevent a build-up of excess pore water pressure during the cycles. A frequency of 0.2 Hz was chosen for the subsequent 10^5 *regular* cycles. The cell pressure was kept constant during the cyclic loading. The values of initial relative density I_{D0} specified for the cyclic tests in the following describe the state before the start of the regular cycles.

Four series of cyclic tests have been performed on the materials KFS, SH20 and SH40 (0 %, 20 % or 40 % coarse

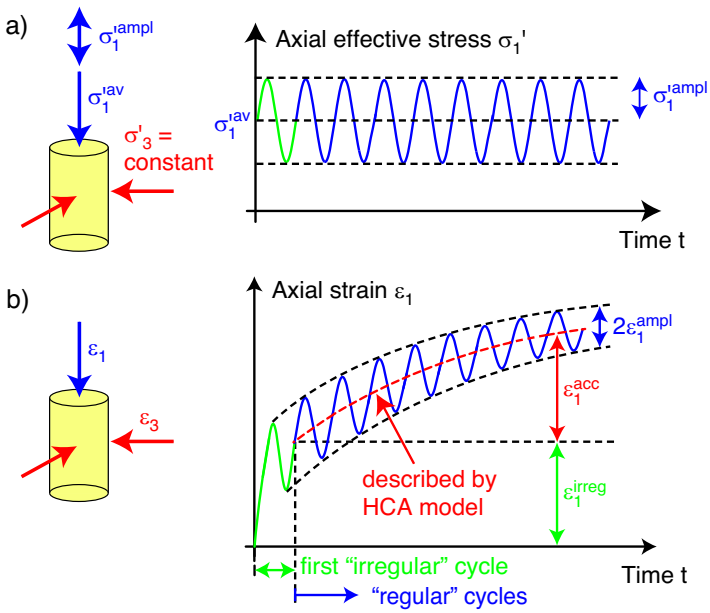

Fig. 5: *a) Axial effective stress σ_1' and b) axial strain ε_1 versus time in a drained cyclic triaxial test*

shell fragments):

1. Variation of stress amplitude q^{ampl} between 20 and 80 kPa, at constant average stress (p^{av} = 200 kPa, η^{av} = 0.75), Figure 6a

2. Variation of initial relative density I_{D0} between loose and dense, keeping the average and cyclic stresses constant (p^{av} = 200 kPa, η^{av} = 0.75, q^{ampl} = 60 kPa), Figure 6b

3. Variation of average mean pressure p^{av} between 50 and 300 kPa, at $\eta^{av} = 0.75$ = constant and with a constant amplitude-pressure ratio $\zeta = q^{ampl}/p^{av} = 0.3$, Figure 6c

4. Variation of average stress ratio η^{av} between 0 and 1.25, under identical values of p^{av} = 200 kPa and q^{ampl} = 60 kPa, Figure 6d. Note that the tests on KFS with q^{ampl} = 40 kPa reported in [103] have been replaced by new tests with q^{ampl} = 60 kPa for the current paper.

Medium dense samples were used in the test series Nos. 1, 3 and 4.

A reduced experimental program, restricted to test series 1 and 2 (variation of q^{ampl} and I_{D0}), has been chosen for the mixtures SH20F (20 % fine shell fragments) and G40 (40 % coarse sand and gravel). Only a single test on a medium dense sample (p^{av} = 200 kPa, η^{av} = 0.75, q^{ampl} = 60 kPa) has been conducted in case of the mixture SH10 (10 % coarse shell fragments).

Since the HCA model predicts the strain accumulation rates due to the regular cycles only, the following discussion of the test data is restricted to the regular cycles. $N = 1$ refers to the end of the first regular cycle. From the initial geometry of a sample (height h_0, volume V_0) and the measured axial displacement Δh and volume change ΔV the axial strain $\varepsilon_1 = \Delta h/h_0$ and the volumetric strain $\varepsilon_v = \Delta V/V_0$ were calculated. The lateral, deviatoric and total strain are obtained from $\varepsilon_3 = 1/2(\varepsilon_v - \varepsilon_1)$,

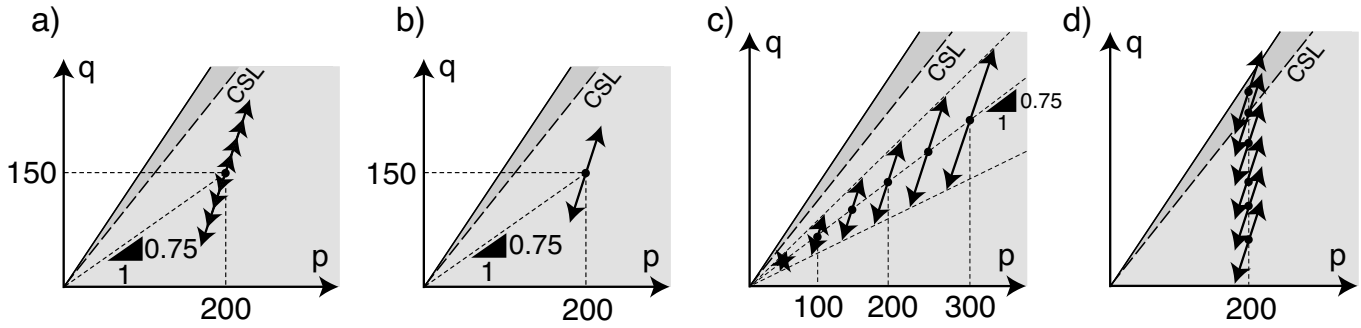

Fig. 6: *Stress paths in the four series of cyclic tests performed on each material shown in the p-q diagram*

$\varepsilon_q = 2/3(\varepsilon_1 - \varepsilon_3)$ and $\varepsilon = \sqrt{{\varepsilon_1}^2 + 2{\varepsilon_3}^2}$. During cyclic loading the various strain components can be splitted into an elastic and a plastic portion, described by the strain amplitude and the accumulated strain ($\varepsilon_1^{\mathrm{ampl}}$ and $\varepsilon_1^{\mathrm{acc}}$ for the axial direction, as shown in Figure 5b). A rate of strain accumulation is defined as the change of strain per cycle, i.e. as the derivative with respect to the number of cycles, e.g. $\dot{\varepsilon}_1^{\mathrm{acc}} = \partial\varepsilon_1^{\mathrm{acc}}/\partial N$. The HCA model (see equations in Appendix) describes the rate of strain accumulation (tensorial quantity) as the product of its *intensity* (scalar quantity) and its *direction* (unit tensor, cyclic flow rule). In the triaxial case, the intensity of stain accumulation is calculated as $\dot{\varepsilon}^{\mathrm{acc}} = \sqrt{(\dot{\varepsilon}_1^{\mathrm{acc}})^2 + 2(\dot{\varepsilon}_3^{\mathrm{acc}})^2}$, while the ratio of volumetric and deviatoric strain rates $\dot{\varepsilon}_v^{\mathrm{acc}}/\dot{\varepsilon}_q^{\mathrm{acc}}$ is a measure of the direction of strain accumulation, with $\dot{\varepsilon}_v^{\mathrm{acc}} = \dot{\varepsilon}_1^{\mathrm{acc}} + 2\dot{\varepsilon}_3^{\mathrm{acc}}$ and $\dot{\varepsilon}_q^{\mathrm{acc}} = 2/3(\dot{\varepsilon}_1^{\mathrm{acc}} - \dot{\varepsilon}_3^{\mathrm{acc}})$. In the following, the test results are first analyzed regarding the direction of accumulation and then with respect to its intensity.

5.1 Direction of strain accumulation

Similar to clean sand [105,109], the direction of strain accumulation has been found independent of amplitude, relative density and average mean pressure for all sand-shell mixtures tested in the present study. As an example data for the mixture SH20 are provided in Figure 7a-c. The direction of the $\varepsilon_q^{\mathrm{acc}}$-$\varepsilon_v^{\mathrm{acc}}$ strain paths remains almost the same although q^{ampl}, I_{D0} and p^{av} are varied from test to test. The decisive parameter for the direction of strain accumulation of both the clean sand and the sand-shell mixtures is the average stress ratio η^{av} (Figure 7d-f). The strain rate ratio $\dot{\varepsilon}_q^{\mathrm{acc}}/\dot{\varepsilon}_v^{\mathrm{acc}}$ increases with η^{av}. This dependence can be well described by the following equation adopted from the flow rule of the Modified Cam clay model:

$$\frac{\dot{\varepsilon}_v^{\mathrm{acc}}}{\dot{\varepsilon}_q^{\mathrm{acc}}} = \frac{{M_{cc}}^2 - (\eta^{\mathrm{av}})^2}{2\eta^{\mathrm{av}}} \quad (1)$$

with $M_{cc} = 6\sin\varphi_{cc}/(3 - \sin\varphi_{cc})$ for triaxial compression tests. M_{cc} corresponds to the stress ratio where the rate of volumetric strain accumulation vanishes, i.e. $\dot{\varepsilon}_v^{\mathrm{acc}} = 0$ while $\dot{\varepsilon}_q^{\mathrm{acc}} \neq 0$. The optimum φ_{cc} values obtained from a curve-fitting of Eq. (1) to the experimental data (see black dashed lines in Figure 7d-f) are summarized in Table 2. Evidently, φ_{cc} grows with increasing shell particle content. As a consequence the mixtures with higher shell particle content show a larger volumetric portion of the strain accumulation rate if tests with an identical average stress ratio η^{av} = 0.75 are compared (Figure 8a), due to the larger distance of the average stress to the line in the p-q plane inclined by $\eta = M_{cc}$.

5.2 Intensity of strain accumulation

The development of accumulated strain $\varepsilon^{\mathrm{acc}}$ with increasing number of cycles N in all tests performed on KFS, SH20 and SH40 is shown in Figure 9. The four rows of diagrams provide the data from the four different test series. In case of the clean KFS the residual strain follows $\varepsilon^{\mathrm{acc}} \sim \ln(N)$ up to $N \approx 10^4$. At larger numbers of cycles the residual strain increases faster than logarithmic with N, i.e. the inclination of the curves in the $\varepsilon^{\mathrm{acc}}$-$N$ diagrams with semi-logarithmic scale increases. The curves $\varepsilon^{\mathrm{acc}}(N)$ of the sand-shell mixtures show a curvature throughout the whole 10^5 applied cycles. Similar tendencies (increasing curvature) have been observed in an earlier test series in case of an increasing uniformity coefficient C_u of the test material [108,110].

The data in Figure 9 reveal that the intensity of strain accumulation grows with stress amplitude q^{ampl} and average stress ratio η^{av}, while it decreases with increasing initial density I_{D0} for all tested materials. Keeping the amplitude-pressure ratio $q^{\mathrm{ampl}}/p^{\mathrm{av}}$ constant leads to almost identical $\varepsilon^{\mathrm{acc}}(N)$ curves for the various average mean pressures p^{av}.

Strain accumulation curves from tests on medium dense samples with identical stresses (p^{av} = 200 kPa, η^{av} = 0.75, q^{ampl} = 60 kPa) are collected in Figure 8b. The cumulative strains grow with increasing content of shell fragments. This is confirmed by the diagrams in Figure 10 presenting the residual strain after 10^5 cycles as a function of q^{ampl}, I_{D0}, p^{av} and η^{av}. In those graphs, for similar relative densities and identical average and cyclic stresses, the residual strain is larger for higher amounts of shell particles. Simultaneously, a reduction of the strain amplitude $\varepsilon^{\mathrm{ampl}}$ with increasing content of shell fragments has been observed, i.e. the granular packing becomes stiffer due to the shells (Figure 11).

The larger strain accumulation rates measured for the mixtures with a higher content of shell fragments seem primarily attributed to the fact that these mixtures are more well-graded (see the grain size distribution curves in Figure 2). This hypothesis is supported by the fact that the mixture G40 with 40 % coarse sand and fine gravel particles of compact shape shows similar cumulative rates as the mixture SH40 with 40 % platy shell fragments. Furthermore, the mixture SH20F with 20 % fine shell fragments, possessing a more uniform gradation, exhibited lower strain accumulation rates than the mixture SH20 with 20 % coarse shell fragments. Therefore, the potential crushability, the

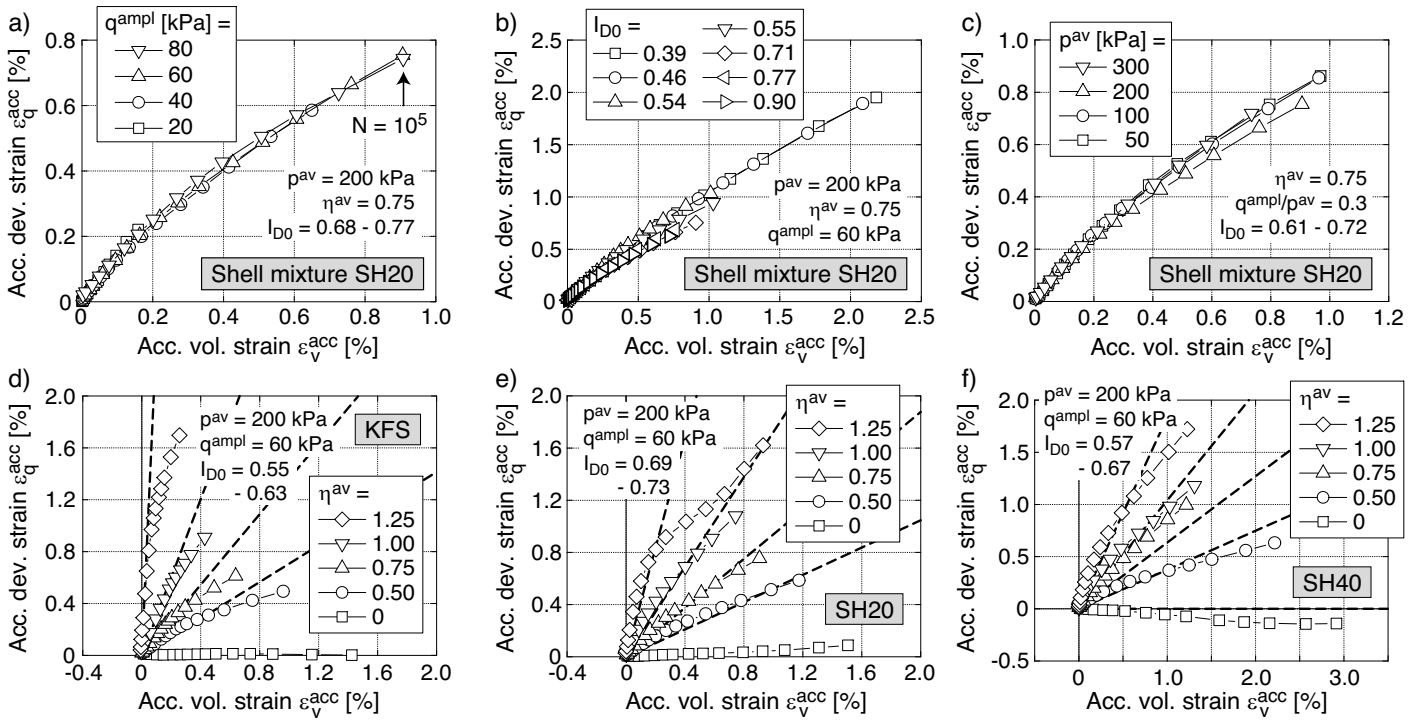

Fig. 7: ε_q^{acc}-ε_v^{acc} *strain paths measured a-c) for the sand-shell mixture SH20 in tests with different stress amplitudes* q^{ampl}*, initial relative densities* I_{D0} *and average mean pressure* p^{av} *or d-f) for KFS, SH20 and SH40 in tests with different average stress ratios* η^{av}*. The dashed lines in diagrams d)-f) have been generated using Eq. (1) with the* φ_{cc} *values in Table 2.*

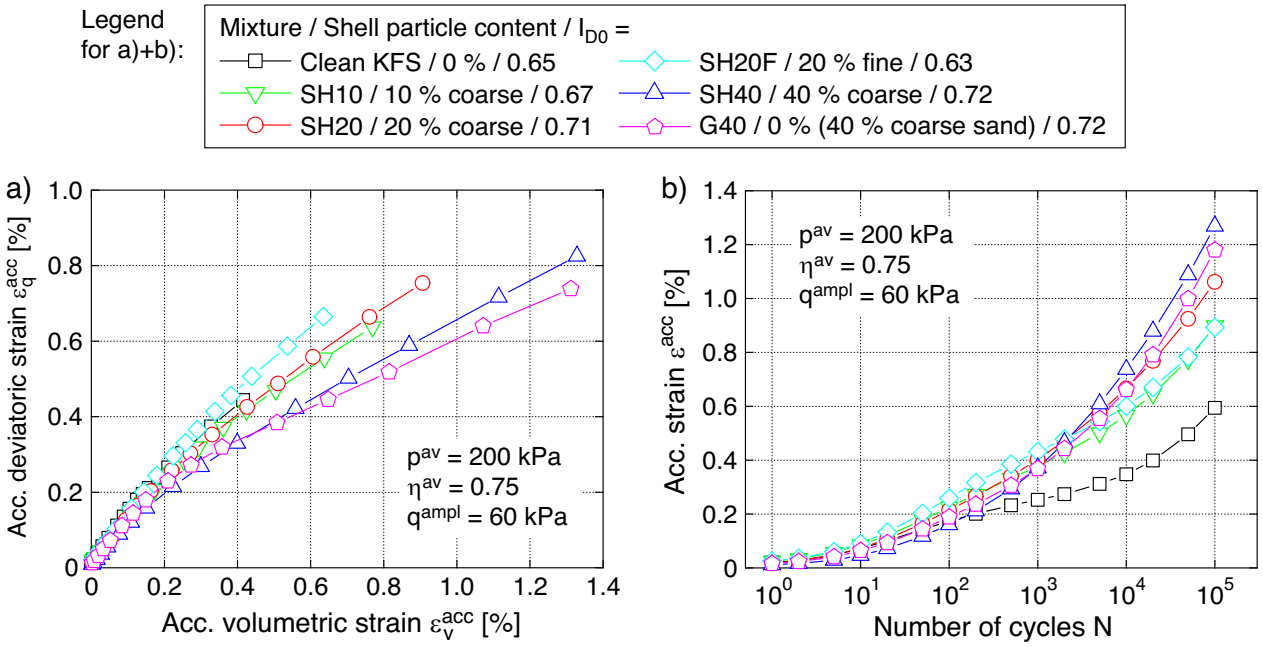

Fig. 8: *Comparison of a)* ε_q^{acc}-ε_v^{acc} *strain paths (direction of strain accumulation) and b) strain accumulation curves* $\varepsilon^{acc}(N)$ *in tests on medium dense samples with identical average and cyclic stresses*

Material	Shell content	φ_{cc} [°]	C_{ampl} [-]	C_e [-]	C_p [-]	C_Y [-]	C_{N1} [10^{-4}]	C_{N2} [-]	C_{N3} [10^{-5}]
KFS	-	32.0	1.33	0.60	0.23	2.10	2.55	0.41	1.9
SH20	20 % coarse	36.2	1.10	0.54	0.11	1.47	13.9	0.045	3.0
SH40	40 % coarse	41.6	0.90	0.39	0.05	2.19	15.8	0.0158	3.1

Table 2: HCA model parameters of clean KFS and sand-shell mixtures SH20 and SH40

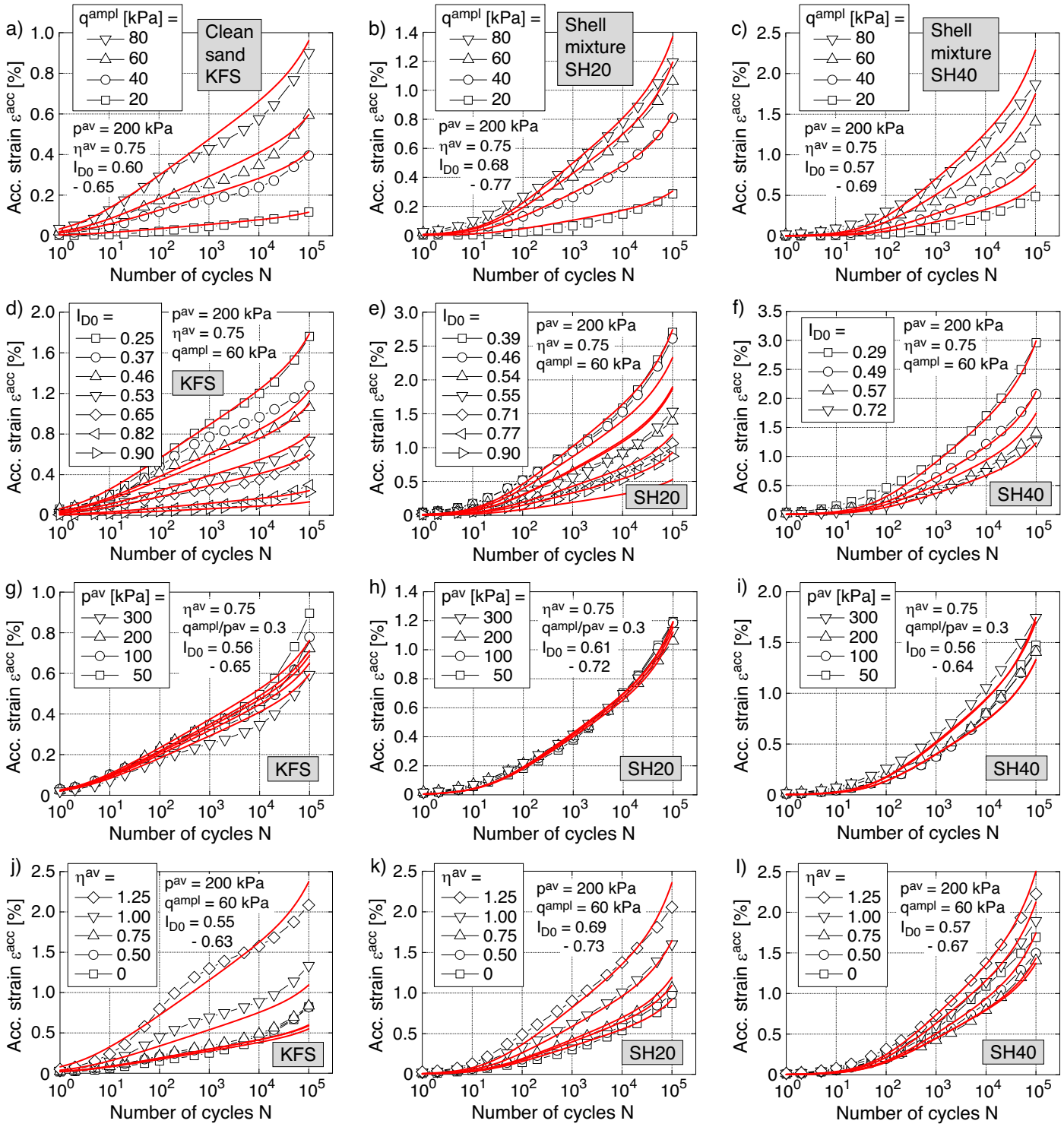

Fig. 9: *Strain accumulation curves $\varepsilon^{acc}(N)$ measured for clean Karlsruhe fine sand (1st column), sand-shell mixture SH20 (2nd column) and mixture SH40 (3rd column) in the four test series with a variation of stress amplitude q^{ampl} (first row), initial relative density I_{D0} (second row), average mean pressure p^{av} (third row) and average stress ratio η^{av} (fourth row)*

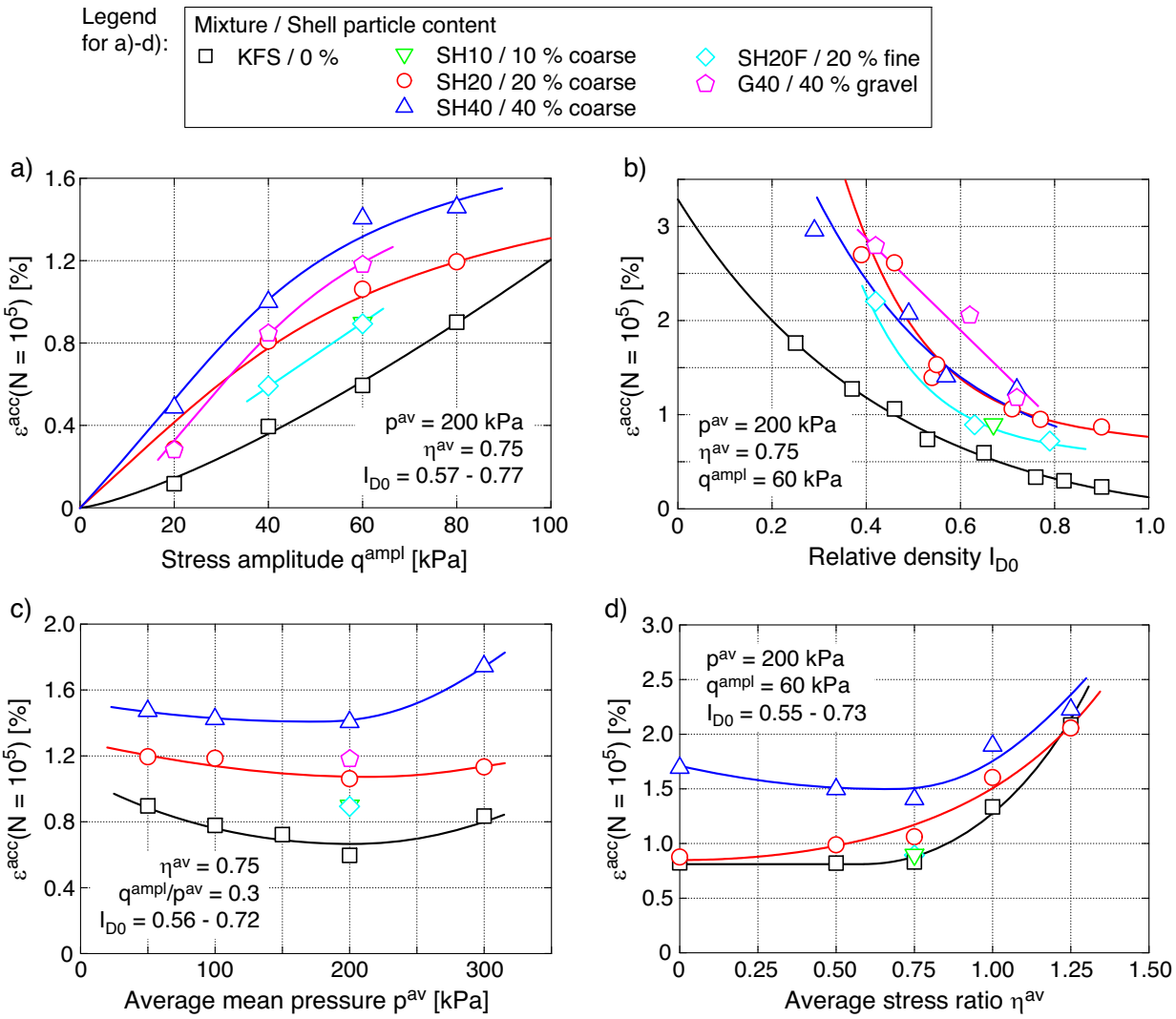

Fig. 10: *Residual strain ε^{acc} after 10^5 cycles as a function of a) stress amplitude q^{ampl}, b) initial relative density I_{D0}, c) average mean pressure p^{av} and d) average stress ratio η^{av}*

platy particle shape of the shell fragments and possible macropores formed by bridging seem to be of secondary importance regarding the cumulative behaviour. Higher strain accumulation rates for clean sands with higher uniformity coefficients have been also observed in [108, 110]. Similar conclusions can be drawn for the elastic portion of strain in Figure 11, where the ε^{ampl} values for SH40 and G40 were close to each other.

5.3 Crushing of shell particles

In order to examine a possible breakage of the shell particles during cyclic loading, a sieve analysis has been performed on the mixture SH40 before and after a cyclic test, in which a medium dense sample was subjected to 10^5 cycles with a large stress amplitude (p^{av} = 200 kPa, η^{av} = 0.75, q^{ampl} = 80 kPa, $\varepsilon^{acc}(N = 10^5) \approx 1.9$ %). The whole mass of the triaxial sample has been sieved once before and once after the test. The grain size distribution curves determined before and after the test were practically identical, giving no hints for particle breakage. The shell fragments involved in the present study are probably too hard to allow for a significant amount of breakage under the applied cyclic loading, in particular when they are embedded into the fine sand matrix.

5.4 HCA model parameters

The HCA model parameters of the clean KFS and the sand-shell mixtures SH20 and SH40 have been derived from the experimental data. The procedure is explained in detail e.g. in [103, 110]. First, a manual calibration of the parameters C_{ampl}, C_e, C_p, C_Y, C_{N1}, C_{N2} and C_{N3} used in the equations for the intensity of accumulation (see Appendix) has been undertaken based on the diagrams in Figure 12. They show the accumulated strain ε^{acc} after different numbers of cycles versus strain amplitude (mean value $\bar{\varepsilon}^{ampl}$ up to the N value under consideration), void ratio (mean value $\bar{e}$ up to N), average mean pressure p^{av} or normalized average stress ratio $\bar{Y}^{av}$ ($\bar{Y}^{av} = 0$ at isotropic average stresses and $\bar{Y}^{av} = 1$ at the critical stress ratio $\eta^{av} = M_{cc}$), respectively. The ε^{acc} data have been purified from the influences of strain amplitude and void ratio by the division with $\bar{f}_{\text{ampl}}$ or $\bar{f}_e$ calculated with $\bar{\varepsilon}^{ampl}$ or $\bar{e}$, respectively. In a second step the parameters derived from Figure 12 have been optimized by means of recalculations of the laboratory tests using an element test program. The red solid curves provided in Figure 9 stem from these simulations using the optimum

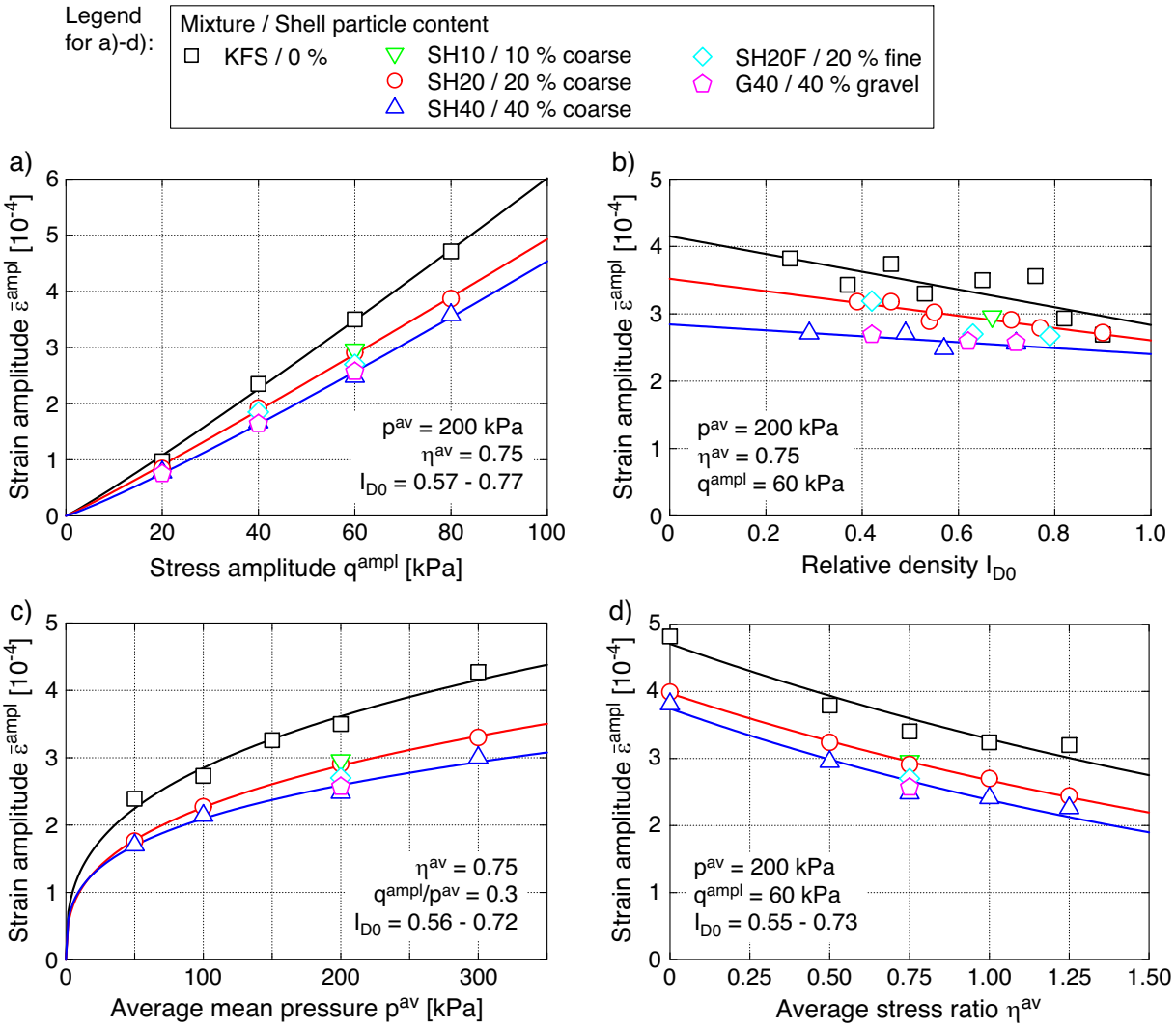

Fig. 11: *Strain amplitude $\bar{\varepsilon}^{ampl}$ (mean values over 10^5 cycles) as a function of a) stress amplitude q^{ampl}, b) initial relative density I_{D0}, c) average mean pressure p^{av} and d) average stress ratio η^{av}*

sets of parameters summarized in Table 2. The relatively low exponents $C_{\text{ampl}} = 1.10$ or 0.90 of the amplitude function for SH20 and SH40 (Table 2) are most striking, being of similar magnitude as values obtained for sands with very angular grains [**?**,103]. A parameter $C_{\text{ampl}} < 1$ means that the rate of strain accumulation $\dot{\varepsilon}^{\text{acc}}$ grows less than proportional with the strain amplitude $\varepsilon^{\text{ampl}}$ (compare Figure 12c).

Figure 13 presents the various HCA model parameters as functions of the shell particle content. While C_{ampl}, C_e, C_p and C_{N2} decrease with increasing content of shells, the opposite tendency is observed for φ_{cc}, C_{N1} and C_{N3}. No clear trend can be concluded for C_Y. Therefore, an increase of the shell particle content leads to a decrease of the dependence of the strain accumulation rate $\dot{\varepsilon}^{\text{acc}}$ on strain amplitude and pressure. The decrease of C_e with increasing shell particle content reflects the overall reduction of void ratios due to the more well-graded grain size distribution curve, keeping in mind that C_e corresponds to the void ratio at $\dot{\varepsilon}^{\text{acc}} = 0$. The tendencies of the parameters C_{Ni} correspond to a more pronounced curvature of the strain accumulation curves $\varepsilon^{\text{acc}}(N)$ in a diagram with semi-logarithmic scale if the sand possesses a larger amount of shell particles.

The platy shell particles lead to a broader grain size distribution curve (Figure 2) and a higher average angularity of the particles in the mixtures. Table 3 compares the trends of the HCA model parameters visible in Figure 13 with the tendencies for increasing values of mean grain size d_{50}, uniformity coefficient C_u and grain angularity detected in the earlier investigations [**?**,103,109,110]. In Table 3 the arrows pointing upwards or downwards mean an increase or a decrease of the respective HCA model parameter with increasing values of d_{50}, C_u, angularity or shell particle content. A minus sign indicates that there is no clear tendency in the available data. As evident from Table 3 most of the trends of the HCA model parameters with increasing shell particle content derived from the present study can be attributed to the broader grain size distribution or the more angular grain shape, respectively, since the tendencies with increasing C_u or grain angularity are the same.

6 Summary, conclusions and outlook

The influence of platy shell particles on the cumulative strains in sand under drained high-cyclic loading has been examined in triaxial tests with 10^5 cycles. Mixtures of Karlsruhe fine sand (KFS) with 10 %, 20 % and 40 % coarse

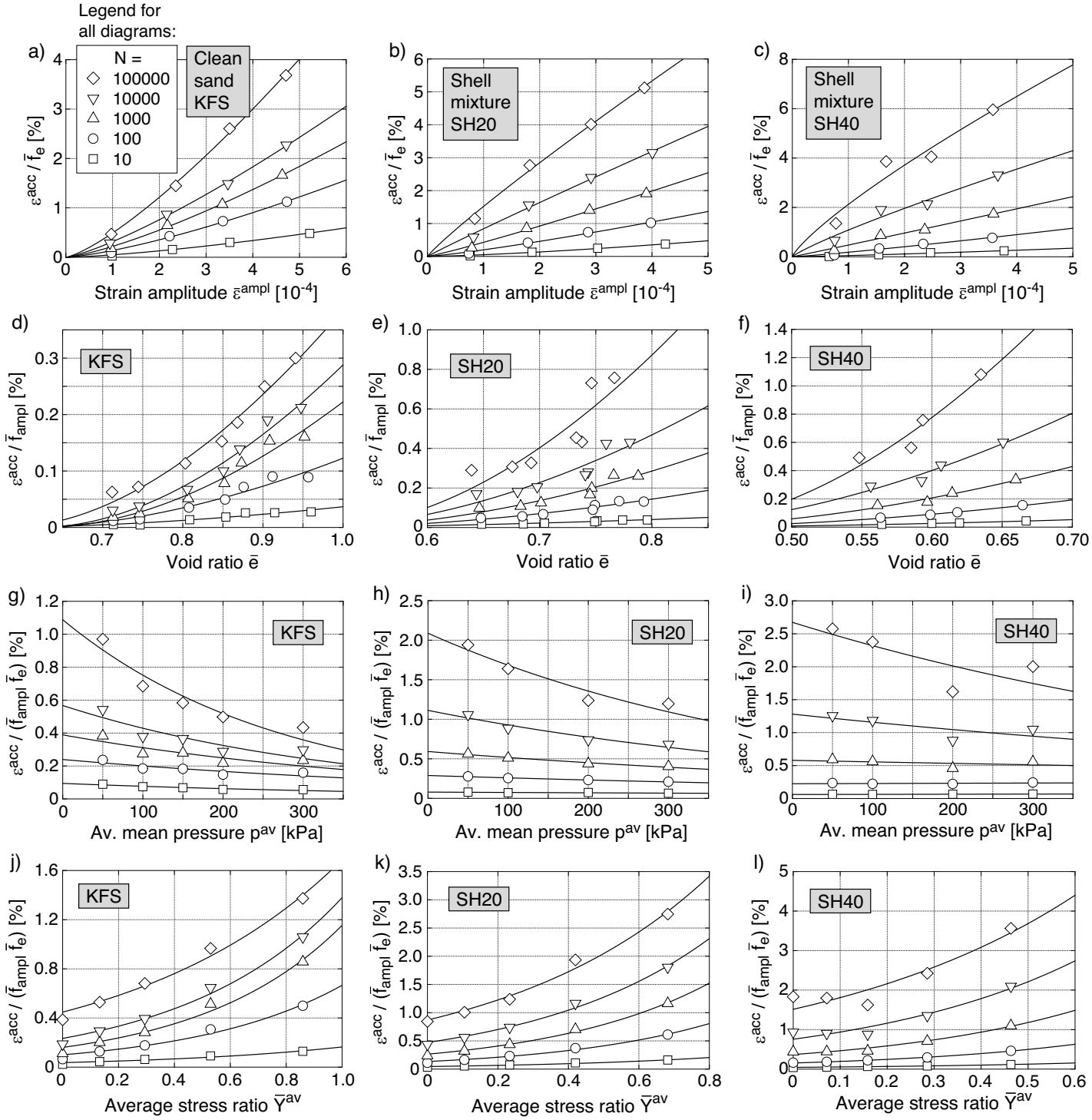

Fig. 12: *Accumulated strain (purified from the influences of strain amplitude and void ratio by the division with $\bar{f}_{ampl}$ and / or $\bar{f}_e$) versus a) strain amplitude $\bar{\varepsilon}^{ampl}$ (mean value up to the cycle number N under consideration), b) void ratio $\bar{e}$ (mean value up to N), c) average mean pressure p^{av} and d) normalized average stress ratio $\bar{Y}^{av}$*

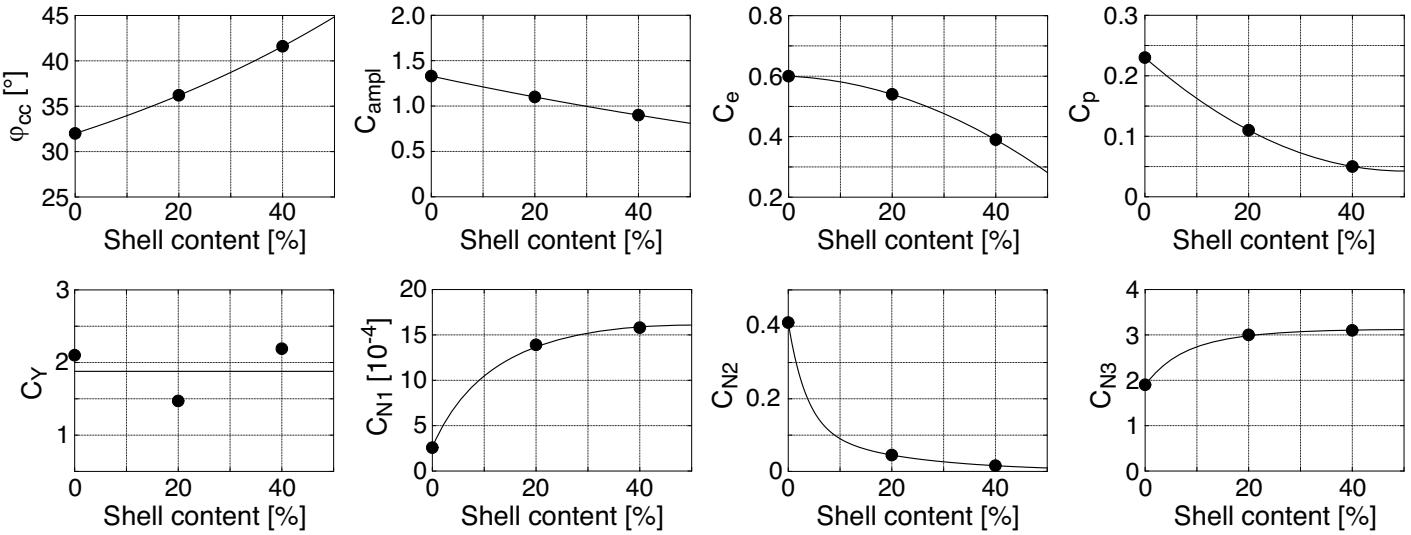

Fig. 13: *Parameters of the HCA model in dependence of the content of shell particles*

HCA model parameter	d_{50} [109, 110]	C_u [109, 110]	Grain angularity [?]	Shell content (this study)
φ_{cc}	↑	↑	↑	↑
C_{ampl}	-	-	↓	↓
C_e	↓	↓	-	↓
C_p	↓	-	↓	↓
C_Y	↑	-	↓	-
C_{N1}	↓	↑	↑	↑
C_{N2}	↑	↓	-	↓
C_{N3}	↓	↑	↓	↑

Table 3: Tendencies of HCA model parameters (↑ = increase of parameter, ↓ = decrease, - = no clear trend) if the mean grain size d_{50}, the uniformity coefficient C_u, grain angularity and shell particle content increases

shell particles (90 % grain sizes in the range 0.6 mm $\leq d \leq$ 8 mm) or 20 % fine shell particles (90 % within 0.2 mm $\leq d \leq$ 2 mm) have been tested. Comparative tests have been also performed on a mixture possessing 40 % coarse sand and fine gravel instead of the coarse shell particles, having the same grain size distribution curve as the 40 % sand-shell mixture. The additional shell particle content renders the grain size distribution curves of the mixtures more well-graded.

Similar to clean sand, the *direction* of strain accumulation (cyclic flow rule) of the sand-shell mixtures, i.e. the ratio of the volumetric and deviatoric strain accumulation rates was found independent of stress amplitude, initial density and average mean pressure. For each tested mixture the strain rate ratio $\dot{\varepsilon}_q^{\text{acc}}/\dot{\varepsilon}_v^{\text{acc}}$ was observed to increase with the average stress ratio η^{av}. This dependence can be sufficiently well described by the flow rule of the Modified Cam clay model.

The *intensity* of strain accumulation increases with growing content of shell particles. Since similar cumulative rates have been measured for the mixtures with 40 % coarse shell particles and 40 % coarse sand and fine gravel, this rise of $\dot{\varepsilon}^{\text{acc}}$ seems primarily attributed to the more well-graded grain size distribution curve of the mixtures possessing larger amounts of coarse particles. Sieve analysis before and after a cyclic test did not show any relevant breakage of the shell particles.

The parameters of the high-cycle accumulation (HCA) model of KFS and the mixtures with 20 % or 40 % coarse shell particles have been calibrated based on the experimental data. Relationships between the parameters and the shell particle content were found similar to the tendencies with uniformity coefficient and grain angularity observed in earlier studies. Amongst others, the exponent C_{ampl} of the amplitude function was found to decrease with increasing shell particle content. The very low value $C_{\text{ampl}} = 0.9$ observed for the 40 % mixture means that the rate of strain accumulation grows less than proportional with strain amplitude.

As a continuation of the current study additional tests on the sand-shell mixtures using moist tamping as the sample preparation method are planned. It can be expected that this method leads to a more random orientation of the platy shell particles. Micromechanical investigations will give insight into the orientation of the shell particles, possible bridging and macropores, and their effect on the cumulative behaviour. The investigations will be also extended to various potentially crushable sands, i.e. calcareous sands or sands of volcanic origin. The cumulative behaviour of these materials and their HCA model parameters will be compared to quartz sands.

Acknowledgements

The presented study has been funded by the German Research Council (DFG, project No. TR 218/18-1 / WI 3180/3-1). The authors are grateful to DFG for the financial support. All tests have been performed by the technicians H. Borowski, P. Gölz and N. Demiral in the soil mechanics laboratory of the Institute of Soil Mechanics and Rock Mechanics (IBF) at Karlsruhe Institute of Technology (KIT).

References

[1] M. M. Ahmadi and N. A. Paydar. Requirements for soil-specific correlation between shear wave velocity and liquefaction resistance of sands. *Soil Dynamics and Earthquake Engineering*, 57:152–163, 2014.

[2] M. Al-Hussaini. Effect of particle size and strain conditions on the strength of crushed basalt. *Canadian Geotechnical Journal*, 20:706–717, 1983.

[3] F.N. Altuhafi and M.R. Coop. Changes to particle characteristics associated with the compression of sands. *Géotechnique*, 61(6):459–471, 2011.

[4] F. Amini and Z. Qi. Liquefaction testing on stratified silty sands. *Journal of Geotechnical and Geoenvironmental Engineering, ASCE*, 126(3):208–217, 2000.

[5] K.H. Andersen. Bearing capacity under cyclic loading - offshore, along the coast, and on land. The 21st Bjerrum Lecture presented in Oslo, 23 November 2007. *Canadian Geotechnical Journal*, 46(5):513–535, 2009.

[6] K.H. Andersen and K. Schjetne. Database of friction angles of sand and consolidation characteristics of sand, silt, and clay. *Journal of Geotechnical and Geoenvironmental Engineering, ASCE*, 139(7):1140–1155, 2013.

[7] G. A. Athanasopoulos and V. C. Xenaki. Discussion of: Liquefaction Susceptibility Criteria for Silts and Clays by Ross W. Boulanger and I. M. Idriss. *Journal of Geotechnical and Geoenvironmental Engineering, ASCE*, (07):1025–1027, 2008.

[8] A. L. Baki, M. M. Rahman, S. R. Lo, and C. T. Gnanendran. Linkage between static and cyclic liquefaction of loose sand with a range of fines contents. *Canadian Geotechnical Journal*, 49:891–906, 2012.

[9] M. H. Baziar and H. Sharafi. Assessment of silty sand liquefaction potential using hollow torsional tests - An energy approach. *Soil Dynamics and Earthquake Engineering*, 31(3):857–865, 2011.

[10] K. Been and M.G. Jefferies. A state parameter for sands. *Géotechnique*, 35(1):99–112, 1985.

[11] M. Belkhatir, T. Schanz, Am Arab, N. Della, and A. Kadri. Insight into the effects of gradation on the pore pressure generation of sand - silt mixtures. *Geotechnical Testing Journal, ASTM*, 37(5):1–10, 2014.

[12] G.D. Bouckovalas, K.I. Andrianopoulos, and A.G. Papadimitriou. A critical state interpretation for the cyclic liquefaction of silty sands. *Soil Dynamics and Earthquake Engineering*, 23:115–125, 2003.

[13] J.A. H. Carraro, P. Bandini, and R. Salgado. Liquefaction resistance of clean and nonplastic silty sands based on cone penetration resistance. *Journal of Geotechnical and Geoenvironmental Engineering, ASCE*, 129(11):965–976, 2003.

[14] J.A.H. Carraro, M. Prezzi, and R. Salgado. Shear strength and stiffness of sands containing plastic or nonplastic fines. *Journal of Geotechnical and Geoenvironmental Engineering, ASCE*, 135(9):1167–1178, 2009.

[15] G. Castro and S.J. Poulos. Factors affecting liquefaction and cyclic mobility. *Journal of the Geotechnical Engineering Division, ASCE*, 103(GT6):501–516, 1977.

[16] I. Cavarretta, M. Coop, and C. O'sullivan. The influence of particle characteristics on the behaviour of coarse grained soils. *Géotechnique*, 60(6):413–423, 2010.

[17] L.-K. Chien, Y.-N. Oh, and C.-H. Chang. Effects of fines content on liquefaction strength and dynamic settlement of reclaimed soil. *Canadian Geotechnical Journal*, 39:254–265, 2002.

[18] G.-C. Cho, J. Dodds, and J.C. Santamarina. Particle shape effects on packing density, stiffness, and strength: natural and crushed sands. *Journal of Geotechnical and Geoenvironmental Engineering, ASCE*, 132(5):591–602, 2006.

[19] J. Chu and W.K. Leong. Effect of fines on instability behavior of loose sand. *Géotechnique*, 52(10):751–755, 2002.

[20] M.R. Coop. The mechanics of uncemented carbonate sands. *Géotechnique*, 40(4):607–626, 1990.

[21] M.R. Coop, K.K. Sorensen, T. Bodas Freitas, and G. Georgoutos. Particle breakage during shearing of a carbonate sand. *Géotechnique*, 54(3):157–163, 2004.

[22] H.K. Dash, T.G. Sitharam, and B.A. Baudet. Influence of non-plastic fines on the response of a silty sand to cyclic loading. *Soils and Foundations*, 50(5):695–704, 2010.

[23] S. Donohue, C. O'Sullivan, and M. Long. Particle breakage during cyclic triaxial loading of a carbonate sand. *Géotechnique*, 59(5):477–482, 2009.

[24] J.-C. Dupla and J. Canou. Cyclic pressuremeter loading and liquefaction properties of sands. *Soils and Foundations*, 43(2):17–31, 2003.

[25] M.D. Evans and S. Zhou. Liquefaction behavior of sand-gravel composites. *Journal of Geotechnical Engineering, ASCE*, 121(3):287–298, 1995.

[26] V.N. Georgiannou. The undrained response of sands with additions of particles of various shapes and sizes. *Géotechnique*, 56(9):639–649, 2006.

[27] D. Giretti, V. Fioravante, K. Been, and S. Dickenson. Mechanical properties of a carbonate sand from a dredged hydraulic fill. *Géotechnique*, 68(5):410–420, 2018.

[28] U. Gori and M. Mari. The correlation between the fractal dimension and internal friction angle of different granular materials. *Soils and Foundations*, 41(6):17–23, 2001.

[29] P. Guo and X. Su. Shear strength, interparticle locking, and dilatancy of granular materials. *Canadian Geotechnical Journal*, 44(5):579–591, 2007.

[30] H. Hanzawa. Undrained strength and stability analysis for a quick sand. *Soils and Foundations*, 20(2):17–29, 1980.

[31] B. Hardin. Crushing of soil particles. *Journal of Geotechnical Engineering, ASCE*, 111(10):1177–1192, 1985.

[32] M. Hatanaka, Y. Suzuki, T. Kawasaki, and M. Endo. Cyclic undrained shear properties of high quality undisturbed Tokyo gravel. *Soils and Foundations*, 28(4):57–68, 1988.

[33] K. Hazirbaba and E. M. Rathje. Pore pressure generation of silty sands due to induced cyclic shear strains. *Journal of Geotechnical and Geoenvironmental Engineering, ASCE*, 135(12):1892–1905, 2009.

[34] C.C. Hird and F. Hassona. Discussion on "A state parameter for sands". *Géotechnique*, 36(1):124–127, 1986.

[35] A.-B. Huang and S.-Y. Chuang. Correlating cyclic strength with fines contents through state parameters. *Soils and Foundations*, 51(6):991–1001, 2011.

[36] Y.-T. Huang, A.-B. Huang, Y.-C. Kuo, and M.-D. Tsai. A laboratory study on the undrained strength of a silty sand from Central Western Taiwan. *Soil Dynamics and Earthquake Engineering*, 24(9-10):733–743, 2004.

[37] M. Hyodo, N. Aramaki, M. Itoh, and A.F.L. Hyde. Cyclic strength and deformation of crushable carbonate sand. *Soil Dynamics and Earthquake Engineering*, 15(5):331–336, 1996.

[38] M. Hyodo, A.F.L. Hyde, and N. Aramaki. Liquefaction of crushable soils. *Géotechnique*, 48(4):527–543, 1998.

[39] K. Ishihara. *Soil Behaviour in Earthquake Geotechnics*. Oxford Science Publications, 1996.

[40] S. Jänke. Zusammendrückbarkeit und Scherfestigkeit nichtbindiger Erdstoffe - ihre quantitative Ermittlung mit Hilfe einfacher Kennwerte und Feststellung der sie bestimmenden Einflußfaktoren. *Baumaschine und Bautechnik*, 15(3):91–101, 1968.

[41] M. E. Karim and M. J. Alam. Effect of non-plastic silt content on the liquefaction behavior of sand - silt mixture. *Soil Dynamics and Earthquake Engineering*, 65:142–150, 2014.

[42] R.M. Koerner. Effect of particle characteristics on soil strength. *Journal of the Soil Mechanics and Foundations Division, ASCE*, 96(SM4):1221–1234, 1970.

[43] T. Kokusho, T. Hara, and R. Hiraoka. Undrained shear strength of granular soils with different particle gradations. *Journal of Geotechnical and Geoenvironmental Engineering, ASCE*, 130(6):621–629, 2004.

[44] T. Kokusho, F. Ito, Y. Nagao, and A. R. Green. Influence of non/low-plastic fines and associated aging effects on liquefaction resistance. *Journal of Geotechnical and Geoenvironmental Engineering, ASCE*, 138(6):747–756, 2012.

[45] S.L. Kramer. *Geotechnical earthquake engineering*. Prentice-Hall, Upper Saddle River, N.J., 1996.

[46] R. Kuerbis, D. Negussey, and Y.P. Vaid. Effect of gradation and fines content on the undrained response of sand. In D.J.A. Van Zyl and S.G. Vick, editors, *Hydraulic fill structures. Geotechnical Special Publications No. 21, ASCE, New York*, pages 330–345, 1988.

[47] R. Kuerbis and Y.P. Vaid. Sand sample preparation - the slurry deposition method. *Soils and Foundations*, 28(4):107–118, 1988.

[48] P. Lade and J. Yamamuro. Effects of non-plastic fines on static liquefaction of sand. *Canadian Geotechnical Journal*, 34(6):918–928, 1997.

[49] P.V. Lade, J.A. Yamamuro, and P.A. Bopp. Significance of particle crushing in granular materials. *Journal of Geotechnical Engineering, ASCE*, 122(4):309–316, 1996.

[50] J. Lee, R. Salgado, and J.A.H. Carraro. Stiffness degradation and shear strength of silty sands. *Canadian Geotechnical Journal*, 41:831–843, 2004.

[51] S.L. Leleu and J.R. Valdes. Experimental study of the influence of mineral composition on sand crushing. *Géotechnique*, 57(3):313–317, 2007.

[52] Q.B. Liu and B.M. Lehane. The influence of particle shape on the (centrifuge) cone penetration test (CPT) end resistance in uniformly graded granular soils. *Géotechnique*, 62(11):973–984, 2012.

[53] S. López-Querol and M.R. Coop. Drained cyclic behaviour of loose Dogs Bay sand. *Géotechnique*, 62(4):281–289, 2012.

[54] H. Matsuoka and T. Nakai. A new failure criterion for soils in three-dimensional stresses. In *Deformation and Failure of Granular Materials*, pages 253–263, 1982. Proc. IUTAM Symp. in Delft.

[55] G.R. McDowell and M.D. Bolton. On the micromechanics of crushable aggregates. *Géotechnique*, 48(5):667–679, 1998.

[56] K. Miura, K. Maeda, M. Fureukawa, and S. Toki. Physical characteristics of sands with different primary properties. *Soils and Foundations*, 37(3):53–64, 1997.

[57] K. Miura, K. Maeda, M. Furukawa, and S. Toki. Mechanical characteristics of sands with different primary properties. *Soils and Foundations*, 38(4):159–172, 1998.

[58] R.M. Mizanur and S.R. Lo. Predicting the onset of static liquefaction of loose sand with fines. *Journal of Geotechnical and Geoenvironmental Engineering, ASCE*, 138(8):1037–1041, 2012.

[59] T.G. Murthy, D. Loukidis, J.A.H. Carraro, Prezzi M., and Salgado R. Undrained monotonic response of clean and silty sands. *Géotechnique*, 57(3):273–288, 2007.

[60] S.A. Naeini and M.H. Baziar. Effect of fines content on steady-state strength of mixed and layered samples of a sand. *Soil Dynamics and Earthquake Engineering*, 24(3):181–187, 2004.

[61] Y. Nakata, A.F.L. Hyde, M. Hyodo, and H. Murata. A probabilistic approach to sand particle crushing in the triaxial test. *Géotechnique*, 49(5):567–583, 1999.

[62] Y. Nakata, M. Hyodo, A.F.L. Hyde, Y. Kato, and H. Murata. Microscopic particle crushing of sand subjected to high pressure one dimensional compression. *Soils and Foundations*, 41(1):69–82, 2001.

[63] Q. Ni, T.S. Tan, G.R. Dasari, and D.W. Hight. Contribution of fines to the compressive strength of mixed soils. *Géotechnique*, 54(9):561–569, 2004.

[64] P.G. Nicholson, R.B. Seed, and H.A. Anwar. Elimination of membrane compliance in undrained triaxial testing. I. Measurement and evaluation. *Canadian Geotechnical Journal*, 30(5):727–738, 1993.

[65] A. Niemunis, T. Wichtmann, and Th. Triantafyllidis. A high-cycle accumulation model for sand. *Computers and Geotechnics*, 32(4):245–263, 2005.

[66] M. Oda. Anisotropic strength of cohesionless sands. *Journal of the Geotechnical Engineering Division, ASCE*, 107(9):1219–1231, 1981.

[67] A. Papadopoulou and T. Tika. The effect of fines on critical state and liquefaction resistance characteristics of nonplastic silty sands. *Soils and Foundations*, 48(5):713–725, 2008.

[68] C. Polito and J. Martin. Effects of nonplastic fines on the liquefaction resistance of sands. *Journal of Geotechnical and Geoenvironmental Engineering, ASCE*, 127(5):408–415, 2001.

[69] C.P. Polito and J.R. Martin. A reconcilation of the effects of non-plastic fines on the liquefaction resistance of sands reported in the literature. *Earthquake Spectra*, 19(3):635–651, 2003.

[70] Md.M. Rahman and S.R. Lo. Undrained behavior of sand-fines mixtures and their state parameter. *Journal of Geotechnical and Geoenvironmental Engineering, ASCE*, 140(7):04014036–1–04014036–12, 2014.

[71] Md.M. Rahman, S.R. Lo, and Md.A.L. Baki. Equivalent granular state parameter and undrained behaviour of sand-fines mixtures. *Acta Geotechnica*, 6(4):183–194, 2011.

[72] M.M. Rahman, S.R. Lo, and C.T. Gnanendran. On equivalent granular void ratio and steady state behaviour of loose sands with fines. *Canadian Geotechnical Journal*, 45(10):1439–1456, 2008.

[73] G.A. Ross, H.B. Seed, and R.R. Migliaccio. Bridge foundations in Alaska earthquake. *Journal of the Soil Mechanics and Foundations Division, ASCE*, 95(SM4):1007–1036, 1969.

[74] P.C. Rousé, R.J. Fannin, and D.A. Shuttle. Influence of roundness on the void ratio and strength of uniform sand. *Géotechnique*, 58(3):227–231, 2008.

[75] A. Sadrekarimi and S.M. Olson. Critical state friction angle of sands. *Géotechnique*, 61(9):771–783, 2011.

[76] M. Salem, H. Elmamlouk, and S. Agaiby. Static and cyclic behavior of North Coast calcareous sand in Egypt. *Soil Dynamics and Earthquake Engineering*, 55(10):83–91, 2013.

[77] R. Salgado, P. Bandini, and A. Karim. Shear strength and stiffness of silty sand. *Journal of Geotechnical and Geoenvironmental Engineering, ASCE*, 126(5):451–462, 2000.

[78] E.A. Sandoval and M.A. Pando. Experimental assessment of the liquefaction resistance of calcareous biogeneous sands. *Earth Science Research Journal*, 16(1), 2012.

[79] H.B. Seed and I.M. Idriss. Simplified procedure for evaluating soil liquefaction potential. *Journal of the Soil Mechanics and Foundations Division, ASCE*, 97(SM9):1249–1273, 1971.

[80] H.B. Seed and W.H. Peacock. Test procedures for measuring soil liquefaction characteristics. *Journal of the Soil Mechanics and Foundations Division, ASCE*, 97(SM8):1099–1119, 1971.

[81] A. Sezer, S. Altun, and B.A. Göktepe. Relationships between shape characteristics and shear strength of sands. *Soils and Foundations*, 51(5):857–871, 2011.

[82] J.T. Shahu and Yudhbir. Model tests on sands with different angularity and mineralogy. *Soils and Foundations*, 38(4):151–158, 1998.

[83] S.S. Sharma and M. Ismail. Monotonic and cyclic behavior of two calcareous soils of different origins. *Journal of Geotechnical and Geoenvironmental Engineering, ASCE*, 132(12):1581–1591, 2006.

[84] H. Shin and J.C. Santamarina. Role of particle angularity on the mechanical behavior of granular mixtures. *Journal of Geotechnical and Geoenvironmental Engineering, ASCE*, 139(2):353–355, 2013.

[85] S. Singh. Re-examination of the effects of fine contents on the liquefaction characteristics of sands. In K. Ishihara, editor, *Earthquake geotechnical engineering*, pages 829–831. Balkema, Rotterdam, The Netherlands, 1994.

[86] C. A. Stamatopoulos. An experimental study of the liquefaction strength of silty sands in terms of the state parameter. *Soil Dynamics and Earthquake Engineering*, 30(2):662–678, 2010.

[87] C.A. Stamatopoulos. Discussion of "The effect of fines on critical state and liquefaction resistance characteristics of non-plastic silty sands" by Papadopoulou & Tika. *Soils and Foundations*, 50(1):173–176, 2010.

[88] B. Sukumaran and A.K. Ashmawy. Quantitative characterisation of the geometry of discrete particles. *Géotechnique*, 51(7):619–627, 2001.

[89] F. Tatsuoka. Impacts on geotechnical engineering of several recent findings from laboratory stress-strain tests on geomaterials. In A.G. Correia and H. Brandl, editors, *Geotechnics for roads, rail tracks and earth structures*. Balkema, A.A., 2001.

[90] K. Terzhagi. Varieties of submarine slope failures. In *Proc. 8th Texas Conf. on Soil Mech. and Found. Engrg., University of Texas at Austin Bureau of Engineering Special Research Publication No. 29*, 1956.

[91] S. Thevanayagam. Effect of fines and confining stress on undrained shear strength of silty sands. *Journal of Geotechnical and Geoenvironmental Engineering, ASCE*, 124(6):479–491, 1998.

[92] S. Thevanayagam and G.R. Martin. Liquefaction in silty soils - screening and remediation issues. *Soil Dynamics and Earthquake Engineering*, 22:1035–1042, 2002.

[93] S. Thevanayagam, T. Shenthan, S. Mohan, and J. Liang. Undrained fragility of clean sands, silty sands, and sandy silts. *Journal of Geotechnical and Geoenvironmental Engineering, ASCE*, 128(10):849–859, 2002.

[94] K. Tokimatsu. System compliance correction from pore pressure response in undrained triaxial tests. *Soils and Foundations*, 30(2):14–22, 1990.

[95] K. Tokimatsu and K. Nakamura. A simplified correction for membrane compliance in liquefaction tests. *Soils and Foundations*, 27(4):111–122, 1987.

[96] I. Towhata. *Geotechnical Earthquake Engineering*. Springer, 2008.

[97] A. Tsomokos and V.N. Georgiannou. Effect of grain shape and angularity on the undrained response of fine sands. *Canadian Geotechnical Journal*, 47(5):539–551, 2010.

[98] T.S. Ueng, C.W. Sun, and C.W. Chen. Definition of fines and liquefaction resistance of Maoluo river soil. *Soil Dynamics and Earthquake Engineering*, 24:745–750, 2004.

[99] Y.P. Vaid, J.C. Chern, and H. Tumi. Confining pressure, grain angularity and liquefaction. *Journal of Geotechnical Engineering, ASCE*, 111(10):1229–1235, 1985.

[100] Y.P. Vaid, J.M. Fisher, R.H. Kuerbis, and D. Negussey. Particle gradation and liquefaction. *Journal of Geotechnical Engineering, ASCE*, 116(4):698–703, 1990.

[101] L.M. Wei and J. Yang. On the role of grain shape in static liquefaction of sand-fines mixtures. *Géotechnique*, 64(9):740–745, 2014.

[102] T. Wichtmann. Explicit accumulation model for non-cohesive soils under cyclic loading. PhD thesis, Publications of the Institute of Soil Mechanics and Foundation Engineering, Ruhr-University Bochum, Issue No. 38, 2005.

[103] T. Wichtmann. Soil behaviour under cyclic loading - experimental observations, constitutive description and applications. Habilitation thesis, Publications of the Institute of Soil Mechanics and Rock Mechanics, Karlsruhe Institute of Technology, Issue No. 181, 2016.

[104] T. Wichtmann, A. Niemunis, and Th. Triantafyllidis. Strain accumulation in sand due to cyclic loading: drained triaxial tests. *Soil Dynamics and Earthquake Engineering*, 25(12):967–979, 2005.

[105] T. Wichtmann, A. Niemunis, and Th. Triantafyllidis. Experimental evidence of a unique flow rule of non-cohesive soils under high-cyclic loading. *Acta Geotechnica*, 1(1):59–73, 2006.

[106] T. Wichtmann, A. Niemunis, and Th. Triantafyllidis. On the influence of the polarization and the shape of the strain loop on strain accumulation in sand under high-cyclic loading. *Soil Dynamics and Earthquake Engineering*, 27(1):14–28, 2007.

[107] T. Wichtmann, A. Niemunis, and Th. Triantafyllidis. Strain accumulation in sand due to cyclic loading: drained cyclic tests with triaxial extension. *Soil Dynamics and Earthquake Engineering*, 27(1):42–48, 2007.

[108] T. Wichtmann, A. Niemunis, and Th. Triantafyllidis. Validation and calibration of a high-cycle accumulation model based on cyclic triaxial tests on eight sands. *Soils and Foundations*, 49(5):711–728, 2009.

[109] T. Wichtmann, A. Niemunis, and Th. Triantafyllidis. Flow rule in a high-cycle accumulation model backed by cyclic test data of 22 sands. *Acta Geotechnica*, 9(4):695–709, 2014.

[110] T. Wichtmann, A. Niemunis, and Th. Triantafyllidis. Improved simplified calibration procedure for a high-cycle accumulation model. *Soil Dynamics and Earthquake Engineering*, 70(3):118–132, 2015.

[111] T. Wichtmann, K. Steller, and Th. Triantafyllidis. On the influence of the sample preparation method on strain accumulation in sand under high-cyclic loading. *Soil Dynamics and Earthquake Engineering (submitted)*, 2018.

[112] R.T. Wong, H.B. Seed, and C.K. Chan. Cyclic loading liquefaction of gravelly soils. *Journal of the Geotechnical Engineering Division, ASCE*, 101(GT6):571–583, 1975.

[113] V.C. Xenaki and G.A. Athanasopoulos. Liquefaction resistance of sand - silt mixtures: an experimental investigation of the effects of fines. *Soil Dynamics and Earthquake Engineering*, 23:183–194, 2003.

[114] Y. Xiao, H. Liu, Q. Chen, Q. Ma, Y. Xiang, and Y. Zheng. Particle breakage and deformation of carbonate sands with wide range of densities during compression loading process. *Acta Geotechnica*, 12(6):1177–1184, 2017.

[115] Y.F. Xu and D.A. Sun. Correlation of surface fractal dimension with frictional angle at critical state of sands. *Géotechnique*, 55(9):691–695, 2005.

[116] J. Yamamuro and K. Covert. Monotonic and cyclic liquefaction of very loose sands with high silt content. *Journal of Geotechnical and Geoenvironmental Engineering, ASCE*, 127(4):314–324, 2001.

[117] J.A. Yamamuro and P.V. Lade. Static liquefaction of very loose sands. *Canadian Geotechnical Journal*, 34(6):905–917, 1997.

[118] J.A. Yamamuro and P.V. Lade. Steady-state concepts and static liquefaction of silty sands. *Journal of Geotechnical and Geoenvironmental Engineering, ASCE*, 124(9):868–877, 1998.

[119] J. Yang and L.M. Wei. Collapse of loose sand with the addition of fines: The role of particle shape. *Géotechnique*, 62(12):1111–1125, 2012.

[120] S.L. Yang, S. Lacasse, and R. Sandven. Determination of the transitional fines content of mixtures of sand and non-plastic fines. *Geotechnical Testing Journal, ASTM*, 29(2):102–107, 2006.

[121] S.L. Yang, R. Sandven, and L. Grande. Steady-state lines of sand-silt mixtures. *Canadian Geotechnical Journal*, 43:1213–1219, 2006.

[122] L. Zhuang, Y. Nakata, U.-G. Kim, and D. Kim. Influence of relative density, particle shape, and stress path on the plane strain compression behavior of granular materials. *Acta Geotechnica*, 9(2):241–255, 2014.

Appendix: Equations of the HCA model

The basic equation of the HCA model reads

$$\dot{\boldsymbol{\sigma}} = \mathsf{E} : (\dot{\boldsymbol{\varepsilon}} - \dot{\boldsymbol{\varepsilon}}^{\mathrm{acc}} - \dot{\boldsymbol{\varepsilon}}^{\mathrm{pl}}) \tag{2}$$

with the stress rate $\dot{\boldsymbol{\sigma}}$ of the effective Cauchy stress $\boldsymbol{\sigma}$ (compression positive), the strain rate $\dot{\boldsymbol{\varepsilon}}$ (compression positive), the accumulation rate $\dot{\boldsymbol{\varepsilon}}^{\mathrm{acc}}$, a plastic strain rate $\dot{\boldsymbol{\varepsilon}}^{\mathrm{pl}}$ (necessary only for stress paths touching the yield surface) and the stress-dependent elastic stiffness E. In the context of HCA models the dot over a symbol means a derivative with respect to the number of cycles N (instead of time t), i.e. $\dot{\sqcup} = \partial \sqcup / \partial N$. Depending on the boundary conditions, Eq. (2) predicts either a change of average stress ($\dot{\boldsymbol{\sigma}} \neq \mathbf{0}$) or an accumulation of residual strain ($\dot{\boldsymbol{\varepsilon}} \neq \mathbf{0}$) or both.

For $\dot{\boldsymbol{\varepsilon}}^{\mathrm{acc}}$ in Eq. (2) the following multiplicative approach is used:

$$\dot{\boldsymbol{\varepsilon}}^{\mathrm{acc}} = \dot{\varepsilon}^{\mathrm{acc}}\, \mathbf{m} \tag{3}$$

Function	Material constants
$f_{\mathrm{ampl}} = \min\left\{ \left(\dfrac{\varepsilon^{\mathrm{ampl}}}{10^{-4}} \right)^{C_{\mathrm{ampl}}} ; 10^{C_{\mathrm{ampl}}} \right\}$	C_{ampl}
$\dot{f}_N = \dot{f}_N^A + \dot{f}_N^B$	C_{N1}
$\dot{f}_N^A = C_{N1} C_{N2} \exp\left[-\dfrac{g^A}{C_{N1} f_{\mathrm{ampl}}} \right]$	C_{N2}
$\dot{f}_N^B = C_{N1} C_{N3}$	C_{N3}
$f_e = \dfrac{(C_e - e)^2}{1+e} \; \dfrac{1+e_{\max}}{(C_e - e_{\max})^2}$	C_e
$f_p = \exp\left[-C_p \left(\dfrac{p^{\mathrm{av}}}{100\ \mathrm{kPa}} - 1 \right) \right]$	C_p
$f_Y = \exp\left(C_Y\, \bar{Y}^{\mathrm{av}} \right)$	C_Y

Table 4: Summary of the functions and material constants of the HCA model

with the *direction* of strain accumulation (flow rule) $\mathbf{m} = \dot{\boldsymbol{\varepsilon}}^{\mathrm{acc}} / \|\dot{\boldsymbol{\varepsilon}}^{\mathrm{acc}}\| = (\dot{\boldsymbol{\varepsilon}}^{\mathrm{acc}})^{\rightarrow}$ (unit tensor) and the *intensity* of strain accumulation $\dot{\varepsilon}^{\mathrm{acc}} = \|\dot{\boldsymbol{\varepsilon}}^{\mathrm{acc}}\|$. The flow rule of the modified Cam clay (MCC) model is applied for $\mathbf{m}$:

$$\mathbf{m} = \left[\frac{1}{3} \left(p^{\mathrm{av}} - \frac{(q^{\mathrm{av}})^2}{M^2 p^{\mathrm{av}}} \right) \mathbf{1} + \frac{3}{M^2} (\boldsymbol{\sigma}^{\mathrm{av}})^* \right]^{\rightarrow} \tag{4}$$

where $\sqcup^{\rightarrow} = \sqcup / \|\sqcup\|$ denotes the normalization of a tensorial quantity. For the triaxial case the critical stress ratio $M = F\, M_{cc}$ is calculated from

$$F = \begin{cases} 1 + M_{ec}/3 & \text{for } \eta^{\mathrm{av}} \leq M_{ec} \\ 1 + \eta^{\mathrm{av}}/3 & \text{for } M_{ec} < \eta^{\mathrm{av}} < 0 \\ 1 & \text{for } \eta^{\mathrm{av}} \geq 0 \end{cases} \tag{5}$$

wherein

$$M_{cc} = \frac{6 \sin \varphi_{cc}}{3 - \sin \varphi_{cc}} \quad \text{and} \quad M_{ec} = -\frac{6 \sin \varphi_{cc}}{3 + \sin \varphi_{cc}} \tag{6}$$

with parameter φ_{cc}.

The intensity of strain accumulation $\dot{\varepsilon}^{\mathrm{acc}}$ in Eq. (3) is calculated as a product of six functions:

$$\dot{\varepsilon}^{\mathrm{acc}} = f_{\mathrm{ampl}}\, \dot{f}_N\, f_e\, f_p\, f_Y\, f_\pi \tag{7}$$

each considering a single influencing parameter (see Table 4), i.e. the strain amplitude $\varepsilon^{\mathrm{ampl}}$ (function f_{ampl}), the cyclic preloading g^A ($\dot{f}_N$), void ratio e (f_e), average mean pressure p^{av} (f_p), average stress ratio η^{av} or $\bar{Y}^{\mathrm{av}}$ (f_Y) and the effect of polarization changes ($f_\pi = 1$ for a constant polarization as in the case of the test series presented in this paper).

The normalized stress ratio $\bar{Y}^{\mathrm{av}}$ used in f_Y is zero for isotropic stresses ($\eta^{\mathrm{av}} = 0$) and one at a stress ratio $\eta^{\mathrm{av}} = M_{cc}$. The function Y of Matsuoka & Nakai [54] is used for that purpose:

$$\bar{Y}^{\mathrm{av}} = \frac{Y^{\mathrm{av}} - 9}{Y_c - 9} \quad \text{with} \quad Y_c = \frac{9 - \sin^2 \varphi_{cc}}{1 - \sin^2 \varphi_{cc}} \tag{8}$$

$$Y^{\mathrm{av}} = \frac{27(3 + \eta^{\mathrm{av}})}{(3 + 2\eta^{\mathrm{av}})(3 - \eta^{\mathrm{av}})} \tag{9}$$

For a constant strain amplitude, the function f_N simplifies to:

$$f_N = C_{N1} \left[\ln(1 + C_{N2} N) + C_{N3} N \right] \tag{10}$$

List of notations

$\boldsymbol{\varepsilon}$	Strain tensor
$\dot{\boldsymbol{\varepsilon}}$	Strain rate tensor
$\dot{\boldsymbol{\varepsilon}}^{\mathrm{acc}}$	Strain accumulation rate
$\dot{\boldsymbol{\varepsilon}}^{\mathrm{pl}}$	Plastic strain rate
ε	Total strain (= $\|\boldsymbol{\varepsilon}\|$, in triaxial case = $\sqrt{{\varepsilon_1}^2 + 2{\varepsilon_3}^2}$)
ε_1	Axial strain
ε_3	Lateral strain
ε_v	Volumetric strain (= $\varepsilon_1 + 2\varepsilon_3$)
ε_q	Deviatoric strain (= $2/3(\varepsilon_1 - \varepsilon_3)$)
$\varepsilon^{\mathrm{acc}}$	Accumulated strain
$\varepsilon_v^{\mathrm{acc}}$	Accumulated volumetric strain
$\varepsilon_q^{\mathrm{acc}}$	Accumulated deviatoric strain
$\dot{\varepsilon}^{\mathrm{acc}}$	Rate/intensity of strain accumulation (= $\partial\varepsilon^{\mathrm{acc}}/\partial N$)
$\dot{\varepsilon}_v^{\mathrm{acc}}$	Rate of volumetric strain accumulation
$\dot{\varepsilon}_q^{\mathrm{acc}}$	Rate of deviatoric strain accumulation
$\varepsilon^{\mathrm{ampl}}$	Strain amplitude
$\bar{\varepsilon}^{\mathrm{ampl}}$	Mean value of $\varepsilon^{\mathrm{ampl}}$ up to N cycles
η	Stress ratio (= q/p)
η_{c-d}	Stress ratio at the onset of dilatancy
η^{av}	Average stress ratio
ϱ_s	Grain density
$\boldsymbol{\sigma}$	Cauchy stress tensor
$\dot{\boldsymbol{\sigma}}$	Cauchy stress rate tensor
σ_1'	Effective axial stress
σ_3'	Effective lateral stress
$\sigma_1'^{\mathrm{ampl}}$	Amplitude of effective axial stress
φ_{cc}	Critical friction angle
φ_P	Peak friction angle
ψ	Dilatancy angle
B	B-value of Skempton
B_r	Breakage ratio of Hardin
C_u	Uniformity coefficient
C_{ampl}	Material constant of HCA model
C_e	Material constant of HCA model
C_p	Material constant of HCA model
C_Y	Material constant of HCA model
C_{N1}	Material constant of HCA model
C_{N2}	Material constant of HCA model
C_{N3}	Material constant of HCA model
d_{50}	Mean grain size
e	Void ratio
e_{min}	Minimum void ratio
e_{max}	Maximum void ratio
$\bar{e}$	Mean value of e up to N cycles
E	Elastic stiffness of HCA model
E_{50}	Young's modulus
F	Factor for critical stress ratio in general case
FC	Fines content
f_{ampl}	Function of HCA model
$\bar{f}_{\mathrm{ampl}}$	f_{ampl} evaluated with $\bar{\varepsilon}^{\mathrm{ampl}}$
$\dot{f}_N$	Function of HCA model
$\dot{f}_N^A$	Function of HCA model
$\dot{f}_N^B$	Function of HCA model
f_e	Function of HCA model
$\bar{f}_e$	f_e evaluated with $\bar{e}$
f_p	Function of HCA model
f_Y	Function of HCA model
f_π	Function of HCA model
g^A	Preloading variable of HCA model
I_D	Relative density (= $(e_{\mathrm{max}} - e)/(e_{\mathrm{max}} - e_{\mathrm{min}})$)
I_{D0}	Initial value of I_D
$\mathbf{m}$	Flow rule of HCA model
M	Critical stress ratio in general case
M_{cc}	Critical stress ratio for triaxial compression
M_{ec}	Critical stress ratio for triaxial extension
N	Number of cycles
p	Mean effective stress (= $(\sigma_1' + 2\sigma_3')/3$)
p_0	Initial mean effective stress
p^{av}	Average mean effective stress
q	Deviatoric stress (= $\sigma_1' - \sigma_3'$)
q^{av}	Average deviatoric stress
q_{max}	Maximum deviatoric stress
q^{ampl}	Deviatoric stress amplitude
Y	Stress ratio
Y^{av}	Average stress ratio
$\bar{Y}^{\mathrm{av}}$	Normalized average stress ratio